UNIVERSITY OF CALIFORNIA
Los Angeles

Light from dark stars and light through dark matter: emission as a tool to study the unseen

A dissertation submitted in partial satisfaction
of the requirements for the degree
Doctor of Philosophy in Astronomy and Astrophysics

by

Veronica Jane Dike

2023

ABSTRACT OF THE DISSERTATION

Light from dark stars and light through dark matter: emission as a tool to study the unseen

by

Veronica Jane Dike
Doctor of Philosophy in Astronomy and Astrophysics
University of California, Los Angeles, 2023
Professor Tommaso Treu, Chair

This thesis presents progress in two subfields of astrophysics, first in galactic astronomy, describing how a large survey of ground-state silicon monoxide emission can probe asymptotic giant branch stellar envelope expansion, and second in observational cosmology, presenting novel constraints on primordial black holes (PBH) as a fraction of dark matter by leveraging strong gravitational lensing. The Galactic project searched the Very Large Array Bulge Asymmetries and Dynamical Evolution (BAaDE) survey for maser and thermal emission from the $J = 1-0, v = 0$ ground vibrational state transition. I present results characterizing these sources as a nearby disk population and derive the expansion velocity of the emission region by fitting thermal components of lines to an emission model. For the small number of sources with corresponding carbon monoxide emission, I find the expansion velocities to be similar for both the thermal SiO and CO, evidence that both emissions are produced in the same region above the star where the gas has reached terminal velocity. In the cosmology portion of the thesis, the objective is to use a flux-ratio analysis to put constraints on intermediate-mass PBH as a possible fraction of dark matter. A population of PBH within

the dark matter halo of a lensing galaxy would affect the magnification, and therefore the flux ratios, of the images in a quadruply-imaged quasar (quad). By forward-modeling the flux ratios using an Approximate Bayesian Computing technique, I obtain a constraint on PBH within the mass range of $10^4 M_\odot < M_{\rm PBH} < 10^6 M_\odot$ being less than 0.17% of the dark matter with 95% confidence. In addition to the flux-ratio anomaly, the gravitational interaction they would exert over cosmic history would create many different observable effects. I present a stronger limit in the above intermediate-mass range by combining limits from indpendent PBH probes. I also discuss the improved constraining power that JWST lenses will have on the flux-ratio anomaly constraint.

The dissertation of Veronica Jane Dike is approved.

Steven R. Furlanetto

Smadar Naoz

Alice E. Shapley

Tommaso Treu, Committee Chair

University of California, Los Angeles

2023

TABLE OF CONTENTS

LIST OF FIGURES

LIST OF TABLES

ACKNOWLEDGMENTS

I thank all my research mentors, especially my advisor Tommaso Treu and my committee members Alice Shapley, Smadar Naoz, and Steve Furlanetto. Thanks to all current and former members of TT group; my work is especially indebted to that of Daniel Gilman and Anna Nierenberg. Thank you to all the early-career scientists who took the time to teach me how to be an astrophysicist, especially Michael Stroh and Ioana Zelko.

I thank all my professors from the University of New Mexico Valencia Campus, the University of New Mexico in Albuquerque, and UCLA. I would like to take the space here to thank Dr. Stephen Klinksiek, whom I can't thank anywhere else anymore. Dr. K., thank you for being a great teacher, mentor, friend, and for lighting a flame in me to pursue a Ph.D. in astrophysics.

I thank my first teachers, my parents, who have supported this thesis with their unconditional love, guidance, countless hours on the telephone, and the right words at the right time.

I thank my fellow UCLA astro grads. Their camaraderie, care, and construction of community made UCLA Astronomy my home. I especially thank my cohort: Ronald Lopez, Kelly Kosmo O'Neil, Tony Pahl, and Sanaea Rose; our friendship will transcend space and time.

This material is based upon work supported by the National Science Foundation Graduate Research Fellowship Program under Grant No. DGE-1650604. Any opinions, findings, and conclusions or recommendations expressed in this material are those of the author and do not necessarily reflect the views of the National Science Foundation. I thank the LSSTC Data Science Fellowship Program, which is funded by LSSTC, NSF Cybertraining Grant #1829740, the Brinson Foundation, and the Moore Foundation; my participation in the program has benefited this thesis.

This work used computational and storage services associated with the Hoffman2 Shared

Cluster provided by UCLA Institute for Digital Research and Education's Research Technology Group. This research is based on measurements made with the NASA/ESA Hubble Space Telescope obtained from the Space Telescope Science Institute, which is operated by the Association of Universities for Research in Astronomy, Inc., under NASA contract NAS 5–26555. These observations are associated with programs GO-15177 and GO-13732. This research made use of the SIMBAD database, operated at CDS, Strasbourg, France. This research made use of data products from the Midcourse Space Experiment. This publication makes use of data products from the Two Micron All Sky Survey, which is a joint project of the University of Massachusetts and the Infrared Processing and Analysis Center/California Institute of Technology, funded by the National Aeronautics and Space Administration and the National Science Foundation. This work has made use of data from the European Space Agency (ESA) mission Gaia (https://www.cosmos.esa.int/gaia), processed by the Gaia Data Processing and Analysis Consortium (DPAC, https://www.cosmos.esa.int/web/gaia/dpac/consortium). Funding for the DPAC has been provided by national institutions, in particular the institutions participating in the Gaia Multilateral Agreement.

Some of the measurements used herein were obtained at the W. M. Keck Observatory, which is operated as a scientific partnership among the California Institute of Technology, the University of California and the National Aeronautics and Space Administration. The Observatory was made possible by the generous financial support of the W. M. Keck Foundation. I recognize the significant cultural role that the summit of Maunakea has always had within the indigenous Hawaiian community. We are fortunate to have had the privilege to conduct observations from this sacred mountain.

I acknowledge the use of the following software packages: Astropy (Astropy Collaboration et al. 2018 & Astropy Collaboration et al. 2013), Colossus (Diemer, 2018), lenstronomy (Birrer & Amara, 2018; Birrer et al., 2021) Matplotlib (Hunter, 2007), NumPy (Walt et al., 2011), pandas (McKinney, 2010), pyHalo (Gilman et al., 2021), SciPy (Virtanen et al., 2020).

I acknowledge that the results presented in this thesis are based upon both published and unpublished works with additional coauthors. Chapter 2 is a version of Dike et al. (2021) which was written in collaboration with Mark Morris, Mike Rich, Megan Lewis, Luis Henry Quiroga-Nuñez, Michael Stroh, Adam Trapp, and Mark Claussen. Chapter 3 is a version of Dike et al. (2023) which was written in collaboration with Tommaso Treu and Daniel Gilman.

VITA

2017 **B.S., Astrophysics**, University of New Mexico, Albuquerque, NM

2019 **M.S., Astronomy and Astrophysics**, UCLA, Los Angeles, CA

2022–2023 **Teaching Assistant**, Department of Physics and Astronomy, UCLA, Los Angeles, CA. Astronomy 180 – Astrophysics Laboratory (Fall 2022), Astronomy 6 – Cosmology: Our Changing Concepts of the Universe (Winter 2023), Astronomy 3 – Nature of the Universe (Spring 2023), Physics 5CL – Physics for Life Sciences Majors: Electricity, Magnetism, and Modern Physics Laboratory (Summer 2023)

2017–present **Graduate Student Researcher**, Department of Physics and Astronomy, UCLA, Los Angeles, CA

PUBLICATIONS

Strong lensing constraints on primordial black holes as a dark matter candidate
Dike, V., Gilman, D., Treu, T., 2023, MNRAS, 522, 4

Ground Vibrational State SiO Emission in the VLA BAaDE Survey
Dike, V., Morris, M. R., Rich, R. M., Lewis, M. O., Quiroga-Nuñez, L. H., Stroh, M. C., Trapp, A. C., Claussen, M. J., 2021, AJ, 161, 3

Detecting pulsar polarization below 100 MHz with the Long Wavelength Array
Dike, V., Taylor, G. B., Dowell, J., Stovall, K., 2020, MNRAS, 496, 3

Bifrost: A Python/C++ framework for high-throughput stream processing in astronomy

Cranmer, M.D., Barsdell, B.R., Price, D.C., Dowell, J., Garsden, H., Dike, V., Eftekhari, T., Hegedus, A.M., Malins, J., Obenberger, K.S., Schinzel, F., Stovall, K., Taylor, G. B., Greenhill, L. J., 2017 JAI, 6, 04

CHAPTER 1

Introduction

This dissertation presents research in two topics. The first topic is ground-state circumstellar SiO emission within the disk of the Galaxy. For the remainder of the thesis, I step out from the galaxy and leverage strong lensing data to place constraints on primordial black holes of intermediate mass.

1.1 Circumstellar SiO in the ground vibrational state

The varied types of emission around asymptotic giant branch (AGB) stars are a useful probe of stellar properties, such as the AGB mass-loss process and stellar velocity. Maser emission and thermal emission lines can provide insight into the physics of the circumstellar envelope. Circumstellar silicon monoxide masers are well-suited to kinematics studies because they are at the same velocity as the source AGB star. SiO can also be observed as thermal emission, in which case the width of the emission line is directly related to the velocity of the expanding stellar envelope. The Bulge Asymmetries and Dynamical Evolution (BAaDE) survey was carried out the aim of studying Galactic bulge kinematics through a radio survey of SiO maser emission, but this survey also provides a wealth of data to use to better understand AGB circumstellar envelopes themselves.

The focus of the first paper in my dissertation is a study of the $J = 1 - 0, v = 0$ emission in the Very Large Array data from the BAaDE survey, with observations at 43,424 MHz.

This is the largest study of SiO $J = 1 - 0, v = 0$ emission to date and contains thermal lines, maser lines, and composite sources. Emission from the SiO ground state transition $J = 1-0, v = 0$ was noted as a thermal feature in Jewell et al. (1991), confirmed to also exist as maser emission by Boboltz & Claussen (2004), and studied further in a small sample by de Vicente et al. (2016). The ground vibrational state transition was chosen for the work in this thesis because of its relative obscurity in the literature and its tendency to be thermal, which lends insight into the AGB star mass-loss physics.

I present the results of this thorough analysis of the $J = 1 - 0, v = 0$ emission, detailing the kinematics and brightness of the host stars as well as the outflow velocities derived for those sources with a thermal emission component. The thermal features are fit with an emission model from Morris (1985) to extract stellar envelope expansion velocities. The statistics of the occurrence of other lines that appear along with the $J = 1 - 0, v = 0$ line are discussed, but conclusions are difficult to draw given the population of $J = 1 - 0, v = 0$ emitters are nearby by necessity because the emission is faint. I also include a comparison to outflow velocities found from OH and CO observations, which provides insight into the region where the SiO that is undergoing this emission is located within the circumstellar envelope.

1.2 Strong lensing constraints on primordial black holes

A major problem in our understanding of the Universe is that we do not know what composes most of the matter within it. What if this dark matter is at least partially composed of black holes? How would we be able to tell? The theory of primordial black holes (PBH), first introduced by Zel'dovich & Novikov (1967) and Hawking (1971), is that in the very early universe, after inflation but while still radiation-dominated, overdensities collapse into black holes (see Sasaki et al. 2018, Khlopov 2010). A population of PBH can be invoked to solve various astrophysical problems (Carr et al., 2023), notably including a straightforward solution to the mystery of dark matter without inventing a particle beyond the Standard

Model of particle physics (Green & Kavanagh 2021, Carr & Kühnel 2020). However, even if the Universe does not present a straightforward solution, PBH could still make up a significant fraction of dark matter along with weakly interactive massive particles (WIMPS), therefore describing a mixed dark matter model. This model allows for a population of intermediate-mass PBH, which could make up a significant fraction of dark matter as well as neatly explain supermassive black hole seeding Carr & Silk (2018).

Strong lensing has the sensitivity to observationally constrain PBH in the intermediate-mass range of 10^4-$10^6 M_\odot$. The distribution of mass within a galaxy halo that is lensing a distant quasar affects the lensed image. Therefore, examining the flux ratios of quadruply-imaged quasars (quads) can probe the substructure of a dark matter halo (Mao & Schneider, 1998). Anomalies in the flux ratios when compared to a smooth model can be attributed to substructure within the lens. Given that PBH act as point-mass deflectors, they would have a strong effect distinct from that of WIMP subhalos. The lens can be forward-modeled with and without the effect of PBH to test for the PBH-induced flux-ratio anomaly.

The second paper in my dissertation presents the results of applying this flux-ratio anomaly technique to the question of PBH as a fraction of dark matter. Given the vast lens model parameter space, the forward-modeling of the flux ratios requires an Approximate Bayesian Computing technique (Rubin, 1984) to sample the posterior without directly computing the likelihood. This technique applied to flux ratio analysis was developed by Gilman et al. (2020b), Gilman et al. (2020a), and Gilman et al. (2019). I adapt this modeling method to include PBH and use the method on eleven quads to obtain a constraint on the fraction of dark matter mass that can be contained in PBH. I detail this method and present the resulting limit.

Other constraints have been placed within the mass sensitivity range of the above flux-ratio anomaly method, including limits from the Lyman-α forest (Afshordi et al., 2003), dynamical disruption of wide-binaries (or the lack thereof) Quinn et al. (2009), and millilensing statistics

(Wilkinson et al., 2001). The value of pursuing a strong lensing constraint is not only in its independence from these other limits that each have their own modeling assumptions, but also in that all this information can be combined to produce a stronger constraint. The third paper in my dissertation presents the result of a joint analysis of these independent limits, and this work also anticipates the improvement upon the previous analysis that will result from additional JWST observations that were carried out in this calendar year. As well as adding new lenses to the pool of those appropriate for a flux-ratio analysis, the new JWST flux ratio data can improve the constraining power of those lenses that already have observations in other wavelengths.

The content of the thesis is presented in the following four chapters. Chapter 2 presents the results of my circumstellar SiO emission project, characterizing the ground-state vibrational SiO transition within the BAaDE survey. Chapter 3 introduces my work in dark matter and PBH, presenting my constraint on PBH mass fraction using the strong lensing flux-ratio analysis technique. Chapter 4 details an extension of my strong lensing work, using new observations and combining multiple PBH probes to improve the constraint.

CHAPTER 2

Ground Vibrational State SiO Emission in the VLA BAaDE Survey

Using a subsample of the Bulge Asymmetries and Dynamical Evolution (BAaDE) survey of stellar SiO masers, we explore the prevalence and characteristics of ^{28}SiO $J = 1 - 0, v = 0$ emission. We identify 90 detections of maser, thermal, or composite ^{28}SiO $J = 1 - 0, v = 0$ emission out of approximately 13,000 candidate spectra from the NSF's Karl G. Jansky Very Large Array (VLA). We find that the detected sources are likely asymptotic giant branch (AGB) stars belonging to a bright, foreground Milky Way stellar disk population. For the 32 sources showing thermal components, we extract values for outflow velocity by fitting thermal line profiles. We find a range of circumstellar envelope expansion velocities, and compare to previously recorded OH and CO expansion velocities. This preliminary survey is already the largest study of stellar ground-vibrational-state SiO masers to date, and will be expanded to include the entire VLA BAaDE dataset when data reduction for the 18,988 target sources is completed.

2.1 Introduction

SiO emission, thought to be produced above the atmospheres of AGB stars in material that has been levitated by stellar pulsations, is a powerful tool for probing the conditions of the AGB circumstellar environment. SiO masers have long been observed in the excited

vibrational states ($v \geq 1$) since their discovery in the Orion nebula by Snyder & Buhl (1974), but, with a few exceptions, they have been found in the circumstellar envelopes of evolved, mass-losing stars.

Originally, the emission found in the ground vibrational state was observed to be thermal (in this paper, "thermal" means unaffected by maser amplification, rather than "thermalized"). The first surveys of stellar SiO emission focused on the $J = 2 - 1, v = 0$ thermal line (Dickinson et al. 1978, Morris et al. 1979). Thermal lines are useful because their line width gives a measure of the local velocity of the stellar outflow, and their line intensity provides a measure of how much of the gas-phase SiO in the extended envelope has survived grain formation (Morris & Alcock, 1977).

Circumstellar masing from the $J = 1-0, v = 0$ state was predicted by the radiative pumping model of Kwan & Scoville (1974). A tentative detection of maser emission from the ground vibrational state ($v = 0$) of ^{28}SiO in NML Cyg was reported by Dickinson et al. (1978). Chandler & de Pree (1995) observed the ^{28}SiO $J = 1 - 0$ ground state transition in the IRc2 star-forming region in Orion, characterizing the emission profile as a combination of maser and thermal. Jewell et al. (1991) found the first stellar SiO emission from the $J = 1-0, v = 0$ state of ^{28}SiO and recorded 12 sources described as thermal but noted that some had spikes that could be maser emission. Boboltz & Claussen (2004) reported ground-state maser emission in at least 5 sources, and, more recently, de Vicente et al. (2016) reported combined profiles of thermal and maser emission in a total of 28 evolved stars. These profiles have a narrow maser spike above a broad base of thermal emission.

SiO masers are known to occur closer to the stellar photosphere than other circumstellar masers such as OH and H_2O. Greenhill et al. (1995) showed with a Very Long Baseline Array study of the AGB star VX Sgr that SiO masers ($J = 1 - 0, v = 1$) are produced just above the photosphere at 1.3 times the stellar radius (see also Diamond & Kemball 2003), but interferometric observations of the spatial distribution of the ground-state maser line

emission indicate that it is produced farther out in the envelope (Boboltz & Claussen, 2004). This is consistent with the infrared pumping model (including both collisions and radiation) of Herpin & Baudry (2000), which predicts the $J = 1 - 0, v = 0$ emission to be farther from the star in regions of lower SiO density.

The pumping mechanism for SiO maser emission, including $v = 0$ maser emission, is not agreed upon. A population inversion from radiative pumping by stellar photons is suggested by the radial alignment of the polarized emission of SiO $J = 1-0, v = 1$ and, $v = 2$ emission (Desmurs et al., 2000). However, a model of collisional pumping is supported by observations of SiO $J = 1-0, v = 1$ and $v = 2$ lines because they arise in the same region of space around the star (Miyoshi et al., 1994). Predictions for $J = 1 - 0, v = 0$ emission from either model are scarce, likely because of the similarly scarce detections.

In this paper, we report a subsample of stars exhibiting SiO $J = 1-0, v = 0$ emission at 43424 MHz from the Bulge Asymmetries and Dynamical Evolution (BAaDE) dataset[1]. BAaDE is the largest survey of stellar SiO maser sources, so we are able to study the largest sample of SiO $J = 1 - 0, v = 0$ emission to date. Our line profiles have a variety of shapes: narrow maser lines, broad thermal lines, and a composite of the two. The survey and our subsample are discussed in section 2.2. In section 2.3, we discuss our method for modeling and fitting our thermal and composite lines. In section 2.4.1, we show our detections and the results of our line fitting, including our stellar expansion velocities. Section 2.4.2 puts our sources in context by examining the characteristics of the subsample and how they compare to other sources in the full BAaDE survey. Section 2.4.2 also relates our calculated line widths with these population characteristics. We summarize and discuss future work in section 2.5.

[1] http://www.phys.unm.edu/~baade/

2.2 Observations and Sample Selection

The BAaDE survey uses the the NSF's Karl G. Jansky Very Large Array (VLA) and Atacama Large Millimeter Array (ALMA) to survey SiO masers in the Milky Way, with the main goal of constraining kinematics of bulge stars by using the masers to measure stellar line-of-sight velocity. The radio frequencies of SiO masers ensure that there is minimum attenuation by dust in the Galactic plane. Each source was observed for 40-50 seconds. The BAaDE VLA frequency range, 42.4 to 43.4 GHz, encompasses the SiO $J = 1 - 0, v = 0, 1, 2, 3$ transitions, with a frequency resolution of 1.7 km s^{-1}. BAaDE observations also include the 86 GHz SiO $J = 2 - 1, v = 0, 1, 2$ emission in the ALMA dataset—a southern sample of stars complementary to that observed with the VLA—as presented by Stroh et al. (2019).

The BAaDE sample was selected using the criterion that the stars fall within the *iiia* region of the Midcourse Space Experiment (MSX) color-color plane, which is most likely to contain stars with oxygen-rich circumstellar envelopes, and therefore SiO masers (Sjouwerman et al. 2009; see also Lewis et al. 2020). The total sample includes 28,062 stars, 18,988 of which were observed with the VLA. For a more detailed description of the survey, see Sjouwerman et al. (2017) and Sjouwerman et al. (2018). For early results showing that the disk and bulge populations of the BAaDE survey are distinct kinematically, see Trapp et al. (2018). The velocity of SiO masers is the same as the stellar velocity (see Jewell et al. (1991)), which makes them a useful probe of bulge kinematics. Statistics of the vibrational SiO line transitions in a subsample of BAaDE sources are explored in Stroh et al. (2018), in which the authors use maser line strength ratios from different vibrational states as a diagnostic of the density of the circumstellar envelope. Moreover, bolometric characteristics as well as the spatial distribution of the BAaDE sample within the solar neighborhood are presented in Quiroga-Nuñez et al. (2020).

In this paper, we use a subset of the VLA dataset to study the ^{28}SiO $J = 1 - 0, v = 0$ line at 43424 MHz. In order to characterize the SiO $v = 0$ lines from the BAaDE survey,

representative lines were first selected by visually inspecting the BAaDE VLA data that had been calibrated and processed by August 2018, corresponding to roughly 2/3 of the final VLA survey size. Based on the characteristics of the $v = 0$ thermal and maser lines seen at 43424 MHz, which are always much weaker than the vibrationally excited transitions, an automatic line-detection algorithm was devised. An interval of 58 MHz (400 km s^{-1}) was searched on each side of the 43423.853 MHz rest frequency. First, this interval was searched for channels of flux density exceeding 5 times the RMS noise. Any secondary peaks are ignored and the highest amplitude channel assumed to be the line center. To search for broad lines specifically, the same frequency interval was first searched for any channels above the 5-σ threshold, and these channels removed from the spectrum. Then the same frequency interval was again searched using a 5-channel window with a detection threshold for the mean amplitude of the channels in the window to be seven times the RMS noise divided by the square root of the number of channels in the window. The search using the 5-channel window was applied on a channel-by-channel basis. The same velocity range was then similarly searched with a 10-channel window, but we counted a detection with either window size as long as the signal-to-noise ratio of the integrated intensity was above seven, as defined above. Most broad-line sources were found with both window sizes.

Both the narrow and broad line-finding algorithms were run on approximately 13,000 BAaDE spectra. The detections were then visually inspected to reject false-positives, leaving a total of 90 significant detections. These detections are shown in Figures 2.6, 2.7, and 2.8 in the Appendix. The galactic coordinates l and b of our detected $v = 0$ sources, corresponding 2 Micron All Sky Survey (2MASS) names, and any corresponding OH or variable star name are listed in Table 2.1. We cross-matched with the database[2] collected by Ladeyschikov et al. (2019) using a 1″ matching radius to the 2MASS coordinates if known (MSX coordinates otherwise) and note whether there are any previously recorded SiO observations.

[2] maserdb.net

Table 2.1: Galactocentric coordinates (degrees) and alternative names for $v = 0$ sources. The rightmost column lists references to any previous SiO maser observations recorded in the database of Ladeyschikov et al. (2019).

Source Name	l	b	2MASS name	OH name	V* name	Ref.
			Maser-only			
ad3a-00230	−4.41	−2.98	J17464903−3415068	OH355.588−02.978		
ad3a-00531	−7.37	3.01	J17145167−3325546	OH352.625+03.014	RW Sco	abcd
ad3a-00562	−4.84	−0.60	J17355922−3321388	OH355.156−00.597		
ad3a-00582	−8.87	5.21	J17021034−3319285			
ad3a-01244	−1.93	−1.74	J17475111−3129244			
ad3a-01758	−1.77	0.12	J17405413−3022380	OH358.235+00.115		c
ad3a-01815	−1.64	0.09				
ad3a-01975	−1.56	0.44	J17400664−3002019			
ad3a-02502	0.17	−1.31	J17511077−2928102			
ad3a-04289	−1.62	3.79	J17270541−2815299			d
ad3a-04410	−0.05	1.59	J17391937−2808357	OH359.946+01.593		
ad3a-04942	1.63	0.20	J17484093−2725587			
ad3a-04944	1.58	0.29	J17481382−2725523			e
ad3a-05408	0.25	4.23	J17300394−2628029		V2311 Oph	
ad3a-05488	4.89	−3.12	J18085198−2616210	OH004.887−03.121		f

Table 2.1: (Continued)

Source Name	l	b	2MASS name	OH name	V* name	Ref.
ad3a-05782	3.10	1.68	J17462494−2525010			
ad3a-06568	4.06	4.05	J17394605−2321241		V545 Oph	
ad3a-07151	5.60	3.39	J17454035−2223291			
ad3a-08004	10.41	0.31	J18072713−1946392			
ad3a-08141	9.89	2.37	J17584623−1913286			
ad3a-08264	12.77	−1.94	J18203699−1847096			
ad3a-08428	12.21	0.38	J18105305−1810076			
ad3a-08663	13.57	−0.30	J18160768−1717563			
ad3a-09257	16.12	−0.28	J18210454−1502362			
ad3a-10192	20.76	−1.47	J18341639−1129291			
ad3a-10275	20.16	0.25	J18265500−1113473			
ad3a-10590	19.73	2.42	J18181792−1035450			
ad3a-11089	23.33	−1.74	J18400377−0920051			
ad3a-11091	24.23	−3.45	J18475335−0919102			
ad3a-11358	24.13	−0.58	J18372231−0805358			
ad3a-11369	23.97	−0.16	J18353454−0802402	OH023.970−00.164		
ad3a-11532	24.21	0.63	J18330976−0727583	OH024.208+00.633		
ad3a-12084	26.12	−0.66	J18412025−0621581			[g]

Table 2.1: (Continued)

Source Name	l	b	2MASS name	OH name	V* name	Ref.
ad3a-12356	27.29	−0.85	J18440895−0524198			
ad3a-12687	28.28	−0.15		OH28.28 −0.15		
ad3a-12759	28.72	−0.58	J18454842−0400462	OH28.7−0.6	V0439 Sct	
ad3a-13063	29.4	−0.51	J18464926−0322330			
ad3a-13192	29.94	−0.87	J18490520−0303361			
ad3a-13249	30.59	−1.62	J18525523−0249236			
ad3a-13536	−147.41	−3.73	J06373133−0123430		SY Mon	bcd
ad3a-13641	33.37	1.10	J18482151−0051232			
ad3a-14145	33.80	−0.24	J18535249+0039313			h
ad3a-15065	40.13	2.42	J18555696+0730302	OH40.1+2.4		
ad3a-15253	44.80	−2.31	J19213663+0927567	OH44.8−2.3		
ad3a-15268	44.27	−0.99	J19155397+0936556		V1839 Aql	
ad3a-17013	71.74	−2.94	J20233617+3215108			
ad3a-17084	72.92	−2.14	J20234087+3340405			
ad3a-17227	83.66	−10.17	J21272829+3641557		V1906 Cyg	
ae3a-00115	0.52	−0.21				
ae3a-00116	0.47	−0.11	J17470929−2835290			
ae3a-00249	23.60	−0.69	J18364758−0836451			

Table 2.1: (Continued)

Source Name	l	b	2MASS name	OH name	V* name	Ref.
ae3a-00272	25.23	0.18	J18364204−0645549			
ae3a-03912	71.91	−34.26				
ce3a-00005	−4.94	−0.70	J17361012−3329407			
ce3a-00142	20.18	−1.70	J18340225−1206501			
ce3a-00147	22.00	0.07	J18310242−0941134	OH021.996+00.072		
ce3a-00163	26.89	0.20	J18394138−0516558			
ce3a-00181	30.89	0.20	J18465890−0143428	OH030.885+00.203		
Thermal−only						
ad3a-00073	−5.41	−2.29	J17412754−3444239			
ad3a-01076	−3.35	−0.32	J17384049−3157182	OH356.64−0.32		bc
ad3a-04662	1.47	−0.37	J17503125−2751565			
ad3a-06634	5.91	1.23	J17542613−2314097		V0774 Sgr	
ad3a-08239	11.72	−0.18	J18115787−1852125		V4724 Sgr	
ad3a-09805	19.82	−2.85	J18373291−1258051			
ad3a-09843	18.27	0.36	J18225398−1251080			
ad3a-11288	25.09	−3.02	J18475454−0821287	OH025.086−03.022		cf
ad3a-11547	24.23	0.64	J18331043−0726170			

Table 2.1: (Continued)

Source Name	l	b	2MASS name	OH name	V* name	Ref.
ad3a-11702	25.33	−0.81	J18402409−0708030			
ad3a-13264	29.42	0.81	J18420843−0245154			c
ae3a-00012	−4.19	0.28	J17340928−3220006			
			Composite			
ad3a-01844	−1.84	0.49	J17391493−3014243	OH358.162+00.490	V1019 Sco	
ad3a-01922	−1.33	−0.04	J17423501−3005419	OH358.667−00.044		d
ad3a-04112	1.10	−0.83	J17512677−2825371	OH001.095−00.832		d
ad3a-04509	2.93	−3.23	J18050223−2801541		V1804 Sgr	bc
ad3a-05214	2.58	−0.43	J17531884−2656374			
ad3a-05396	4.97	−3.74	J18112756−2629324	OH5.0 −3.8		
ad3a-06531	6.66	−0.45	J18022487−2325161			
ad3a-07589	8.93	−0.01	J18053549−2113422	OH008.933−00.014		bc
ad3a-07741	6.52	4.98	J17415458−2047055			f
ad3a-07850	9.54	0.77				
ad3a-09606	17.55	−0.13	J18231790−1342473	OH017.551−00.126		bcd
ad3a-12266	26.58	−0.11	J18401349−0542113			
ad3a-12641	27.93	0.24	J18412530−0420320		V0646 Sct	d

Table 2.1: (Continued)

Source Name	l	b	2MASS name	OH name	V* name	Ref.
ad3a-13434	30.82	−0.16	J18480882−0156540	OH030.823−00.156		[d]
ad3a-13789	32.06	2.56	J18395534−0018426			
ae3a-00123	0.55	−0.06	J17470898−2829561			
ce3a-00110	8.34	−1.00	J18080404−2213266	OH008.344−01.002	VX Sgr	[abcd]
ce3a-00127	14.17	−0.06	J18162603−1639563		V5102 Sgr	[bc]
ce3a-00172	28.45	0.13	J18424805−0355396			
ce3a-00180	30.94	−0.16	J18482194−0150363			

[a] Cho et al. (1996)

[b] Kim et al. (2010)

[c] Kim et al. (2014)

[d] Ladeyschikov et al. (2019)

[e] Fujii et al. (2006)

[f] Deguchi et al. (2007)

[g] Deguchi et al. (2004)

[h] Deguchi et al. (2010)

2.3 Methods

We fit our thermal SiO lines to the model for thermal emission profiles from spherically symmetric envelopes expanding at constant velocity developed in Morris (1985) (after Sobolev 1960 and Morris 1975):

$$T_b(v_z) = T_0 \frac{\left(1 - \left[\frac{v_z - v_c}{V}\right]^2\right)\left(1 - \exp\left[-\alpha\left(1 - \left[\frac{v_z - v_c}{V}\right]^2\right)^{-1}\right]\right)}{1 - \exp(-\alpha)}, \tag{2.1}$$

in which T_b is the measured brightness temperature, v_z is the velocity of each channel, T_0 is the brightness temperature at the height of the center of the profile, v_c is the velocity at the center of the profile (and hence the line-of-sight velocity of the star), V is the expansion velocity of the stellar envelope, and α is an opacity term parameterizing the shape of the profile which becomes parabolic (concave down) in the optically thick limit and flat-topped in the optically thin limit. This model assumes that the profile is symmetric and that the source is unresolved in most cases.

To perform this fit, we first converted our data from flux density as a function of observing frequency to brightness temperature as a function of velocity. We used the following version of the Rayleigh-Jeans equation to convert from flux density S_ν to brightness temperature:

$$T_b = \frac{2 S_\nu c^2}{\pi k \nu^2 \theta^2} = 5.05 \times 10^5 S_\nu(\mathrm{Jy}), \tag{2.2}$$

where c is the speed of light, k the Boltzmann constant, ν the observing frequency of each channel, and θ is the half-power beam width. Here we use the estimate of θ to be 0.043 arcseconds for the VLA Q-band in A configuration, which we use because we are assuming the sources are unresolved, instead of using the value for the C or D configurations, which

were the actual observing configurations. We converted the frequency of each channel to velocity using the Doppler equation, $v_z = c(\nu - \nu_0)\nu_0^{-1}$, in which the rest frequency of the $J = 1 - 0, v = 0$ line (43423.853 MHz) is ν_0.

The four-parameter Equation 2.1 was fit to the profiles using the nonlinear least-squares fitter CURVEFIT[3] in IDL 8.7. Sources with combined profiles—those with a maser spike above a plateau of thermal emission—were fit after zero-weighting the maser emission, i.e. not allowing those points that are part of the maser spike to influence the fit. Sources showing only thermal emission were fit without modification. Velocities were converted to the local standard of rest at the end of the process.

2.4 Results

2.4.1 Model Fits

We identified 90 total sources of ground-state emission. Of these, 58 have only narrow maser emission (Figure 2.6). We successfully fit Equation 2.1 to the remaining 32 sources exhibiting thermal emission, 20 of which also show maser emission. Figures 2.7 and 2.8 in the Appendix present the spectra of the thermal and composite sources, respectively.

In Table 2.2 we report the values of our model fits of parameters T_0, α, and v_c. The errors reported are the 1σ standard deviations from CURVEFIT. In the cases where there is maser emission that is zero-weighted for the fit, we caution about the value of our opacity parameter α for the shape of the line profile because a significant portion of the center of the line profile is missing. A complete study of opacity would require using more than one rotational transition, and brightness temperature varies with the phase of the stellar oscillation for our sources, so these parameters are reported for completeness but not discussed further in this paper. For profiles with both maser and thermal components, our values of v_c coincide

[3] https://www.harrisgeospatial.com/docs/curvefit.html

with the velocity of the maser peak in most cases, which indicates that the profiles are symmetric as we assumed and that the maser velocity is a good indicator of the stellar velocity. The outliers are ad3a-01844, ad3a-06531, ad3a09606, and ce3a-00127 (see Figure 2.8). The interpretation of the profiles is ambiguous as to whether the maser is truly offset or there is noise at the edge of the thermal pedestal.

The most relevant parameter obtained from our fitting process is V, the expansion velocity of the circumstellar envelope, which is shown in Table 2.3, along with previously derived values of expansion velocity from OH and CO observations. In the model we adopt from Morris (1985), V is half the full width at zero intensity of the thermal line in km s^{-1} because the outflow is assumed to be symmetric about the velocity of the star itself. Out of 8 OH expansion velocities matched to those in Sevenster et al. (1997) and Sevenster et al. (2001), 3 are consistent within 1σ. Furthermore, our SiO outflow velocities coincide with the CO outflow velocities of the 4 sources matched to Josselin et al. (1998).

Sources with only a thermal component are shown in Figure 2.7, and sources with both thermal and maser components are shown in Figure 2.8.

Table 2.2: Three of the four parameters from our fit, using the thermal emission model of Morris (1985). The fourth parameter, V, is shown in Table 2.3. T_0 is brightness temperature, α is the opacity parameter, and v_c is the local standard of rest velocity of the star, which has an intrinsic error of about 1 km s^{-1}. The fourth column shows signal-to-noise ratio of the integrated intensity. The number in parentheses is the 1σ error in the last digit.

Source Name	T_0 10^3K	α	v_c km s^{-1}	SNR
Thermal-only				
ad3a-00073	28(2)	0.9(5)	-111(1)	9.0

Table 2.2: (Continued)

Source Name	T_0 10^3K	α	v_c km s^{-1}	SNR
ad3a-01076	28(4)	1.7(8)	6(1)	7.3
ad3a-04662	54(2)	4(3)	11.1(3)	7.8
ad3a-06634	36(3)	0.6(4)	-2.2(8)	17.3
ad3a-08239	32(4)	0.6(6)	-37(1)	8.1
ad3a-09805	23(5)	1^{+7}_{-1}	65.3(8)	7.2
ad3a-09843	19.(3)	32(15)	37(1)	7.6
ad3a-11288	24(2)	1.1(8)	8.0(8)	8.3
ad3a-11547	43(3)	13(6)	47.8(7)	19.9
ad3a-11702	19.1(6)	0.20(6)	78.6(2)	9.6
ad3a-13264	25(2)	0.7(5)	56.0(8)	17.0
ae3a-00012	21(3)	1.1(9)	-99(2)	7.4
Composite				
ad3a-01844	35(5)	3(1)	4(1)	10.3
ad3a-01922	34.3(8)	2.6(7)	-3.1(3)	13.8
ad3a-04112	50(2)	0.5(1)	10.2(2)	8.8
ad3a-04509	62(11)	9(6)	30.1(6)	9.1
ad3a-05214	33(5)	2(1)	-1(2)	12.1
ad3a-05396	21(3)	1.0(9)	28(1)	7.7
ad3a-06531	12(9)	0.6(3)	12.0(6)	7.5
ad3a-07589	29(1)	1.0(2)	13.5(6)	12.3
ad3a-07741	33(4)	30(28)	32.1(7)	12.1
ad3a-07850	121(15)	4(1)	13.4(5)	13.6

Table 2.2: (Continued)

Source Name	T_0 10^3K	α	v_c km s^{-1}	SNR
ad3a-09606	80(2)	0.32(5)	44.3(1)	15.1
ad3a-12266	20.2(7)	0.15(6)	-41.1(2)	8.3
ad3a-12641	96(6)	11(3)	52.1(6)	18.0
ad3a-13434	30(2)	1.0(5)	93.2(6)	11.1
ad3a-13789	31.3(9)	0.8(1)	-44.1(3)	10.9
ae3a-00123	73(9)	9(4)	-24.8(9)	13.6
ce3a-00110	143(2)	1.8(2)	7.4(2)	16.9
ce3a-00127	34(2)	0.6(2)	49.9(8)	15.0
ce3a-00172	12(2)	0.6(6)	82(1)	10.1
ce3a-00180	33(4)	0.8(7)	91.7(9)	23.5

Table 2.3: Expansion velocity parameter V from fitting our profiles along with expansion velocities from previous observations of OH (Sevenster et al. 1997 and Sevenster et al. 2001) and CO (Josselin et al., 1998).

Source Name	V	$V_{\rm OH}$	$V_{\rm CO}$
Thermal-only			
ad3a-00073	28(2)	–	–
ad3a-01076	18(2)	–	–
ad3a-04662	11.4(3)	–	–
ad3a-06634	29(1)	–	30.6 (1-0), 30.4 (2-1)
ad3a-08239	12(1)	–	–

Table 2.3: (Continued)

Source Name	V	$V_{\rm OH}$	$V_{\rm CO}$
ad3a-09805	6(6)	–	–
ad3a-09843	19(2)	–	–
ad3a-11288	15.1(9)	13.6	
ad3a-11547	28(1)	–	27.6 (2-1)
ad3a-11702	16.6(2)	–	–
ad3a-13264	25(1)	–	–
ae3a-00012	30(3)	–	–
Composite			
ad3a-01844	20(2)	19.7	–
ad3a-01922	26.1(4)	21.9	–
ad3a-04112	9.9(2)	19.7	–
ad3a-04509	14(1)	–	–
ad3a-05214	28(2)	–	–
ad3a-05396	20(1)	–	–
ad3a-06531	13.7(7)	–	–
ad3a-07589	29.5(6)	4.6	
ad3a-07741	15(1)	–	16.0 (1-0), 18.0 (2-1)
ad3a-07850	15(1)	–	–
ad3a-09606	14.1(2)	14.8	–
ad3a-12266	18.2(2)	–	–
ad3a-12641	30(1)	–	–
ad3a-13434	15.2(7)	20.5	–
ad3a-13789	21.5(4)	–	–

Table 2.3: (Continued)

Source Name	V	$V_{\rm OH}$	$V_{\rm CO}$
ae3a-00123	24(2)	–	–
ce3a-00110	24.3(2)	19.3	22 (2-1)
ce3a-00127	30(1)	–	–
ce3a-00172	18(1)	–	–
ce3a-00180	32(2)	–	–

2.4.2 Population Characteristics

We find evidence that our $J = 1-0, v = 0$ sources belong to the Milky Way stellar disk. The locations of our detections, along with all the BAaDE pointings to which our line-finding algorithm has been applied, are shown in Figure 2.1. There is no latitudinal clustering of our sources in a specific region of the sky, which is better seen in Figure 2.2, which shows the locus of the majority of our sources toward the central region of the Galaxy. As shown in Figure 2.3, our sources tend to be brighter than the main locus of the BAaDE population. This characteristic is consistent with that of the 'kinematically cold' population in the work of Trapp et al. (2018), in which stars in the BAaDE sample with Ks magnitude < 5.5 are found to have a lower collective velocity dispersion and a smaller velocity gradient because of Galactic rotation than stars with Ks > 5.5. This is supported by examining the galactocentric velocities of our population as a function of Galactic longitude in Figure 2.4. We also plot the slope of the rotation trend in longitude, fitting a line in velocity-longitude space to our sources. The rotation slope we measure, 5.73 km s^{-1} deg^{-1}, is consistent with the model of foreground disk stars in Trapp et al. (2018) as well as with the rotation slope of the 'kinematically cold' BAaDE population of approximately 5.5 km s^{-1} deg^{-1} identified therein to be foreground stars in the thick disk. The 'kinematically hot' population has a

slope of 9 km s^{-1} deg^{-1} and primarily consists of members of the Galactic bulge. The fact that our sample of stars with v=0 emission detected can be ascribed to a foreground disk population could result from a selection effect, given that $v = 0$ emission is weak compared to the $J = 1 - 0, v = 1, 2, 3$ masers so we see only nearby sources.

We were able to find 9 distance estimates using matches to the *Gaia* DR2 sample (Gaia Collaboration et al. 2016, Gaia Collaboration et al. 2018), assuming no priors when the relative parallax error was less than 20% (Bailer-Jones, 2015), shown in Table 2.4. The distances, almost entirely within a kiloparsec, are consistent with the hypothesis that our sample of stars is in the foreground. From this matching, we also find that three sources are classified by *Gaia* as Mira variables: ad3a-00531, ad3a-09606, and ce3a-00127. The crossmatch between *Gaia* and BAaDE and the subsequent extraction of distances is the subject of a separate study (Quiroga-Nuñez et al., submitted).

Table 2.4: Distance estimates from *Gaia* parallax measurements.

Source Name	Distance (pc)	Distance Error (pc)
ad3a-00230	478	74
ad3a-00531	514	54
ad3a-08239	683	110
ad3a-09606	981	190
ad3a-10192	737	144
ad3a-12641	1078	170
ad3a-13536	539	70
ad3a-13789	548	99
ce3a-00127	828	131

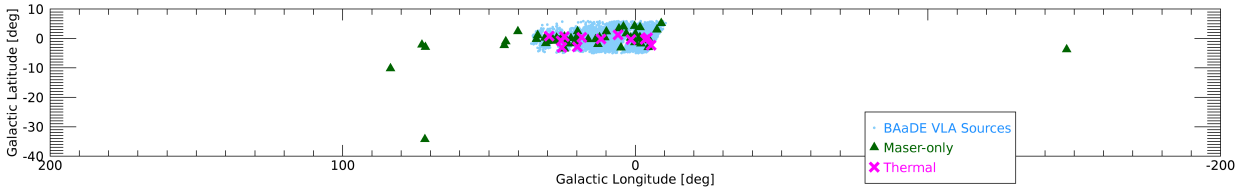

Figure 2.1: Distribution of maser and thermal sources on the sky, along with the current BAaDE VLA survey detections. Outlying maser sources are from observing runs not yet fully reduced.

We found no correlation with the apparent MSX-D magnitude (15 μm). This indicates that the brightness of a source does not correlate with the expansion velocity.

All of our sources also express at least one other maser from higher vibrational states, including the $v = 1, 2$, or 3 states of ^{28}SiO, and in a majority of cases, the ^{29}SiO $v = 0$ maser. We find the fraction of ^{29}SiO $v = 0$, ^{29}SiO $v = 1$, and ^{30}SiO $v = 0$ masers present in our sample to be higher than that of the greater BAaDE survey. For our sources, 74% have a ^{29}SiO $v = 0$ line, 2% have a ^{29}SiO $v = 1$ line, and 38% have a ^{30}SiO $v = 0$ line, compared to 15%, 0.5%, and 2% detection rate, respectively, in BAaDE sources that have a ^{28}SiO $v = 1$ line. Fluxes for isotopologue lines in the BAaDE survey will be published in Sjouwerman et al. (2020, in prep). Our higher fractions can be explained by the fact that these lines are also weak, so sources that are strong enough to display ^{28}SiO $v = 0$ emission are often also strong enough to detect any isotopologue emission that may be present. However, we cannot rule out a pumping mechanism may be favorable to both $J = 1 - 0, v = 0$ emission and these isotopologue lines.

2.5 Discussion and Conclusions

We have presented a study of 43 GHz SiO $J = 1 - 0, v = 0$ emission in the BAaDE survey. Our sample size of 90 sources expands the sample examined in previous studies of SiO

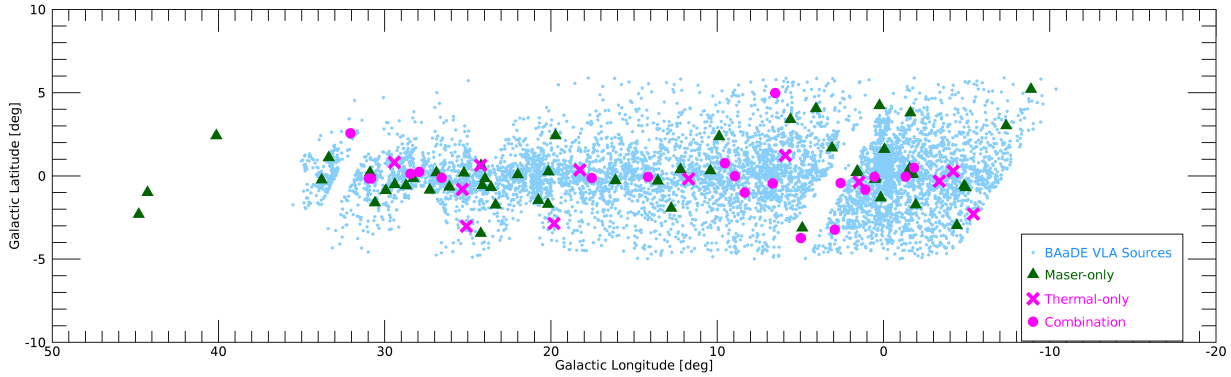

Figure 2.2: An expanded view of the inner part of Figure 2.1, where most of our sources are located.

$J = 1 - 0, v = 0$ maser emission (de Vicente et al. 2016 was previously the largest with a total of 28 sources). For the composite sources, our profiles are consistent with those of de Vicente et al. (2016); we see the maser component centered on the stellar velocity, and we find composite profiles to be common. We find a wider variety of expansion velocities for our stars, as shown in Figure 2.5. We also include one source from Jewell et al. (1991) that was not observed in de Vicente et al. (2016) or our sample, OH 2.6-0.4. The expansion velocities of the de Vicente et al. (2016) sources were estimated by eye based on those published profiles. We share two sources in common with this sample: ad3a-15253 (OH44.8-2.3), which we identify as a maser source, and ce3a-00110 (VX Sgr); our profile with a broad base and a maser peak looks similar to that in de Vicente et al. (2016), and our rough estimate of the expansion velocity of that source based on the profile in de Vicente et al. (2016) is the same, about 24 km s^{-1}. Our value is consistent with the measurement by Jewell et al. (1991) of 24.1 km s^{-1}. The overall lower expansion velocities of de Vicente et al. (2016) compared to our sources could be explained by the fact that those sources were optically selected and not necessarily in the same iiia region of MSX color space as our sources, and therefore not at the same mass-loss stage.

We are able to derive expansion velocities using a thermal emission model fit to the 32 profiles

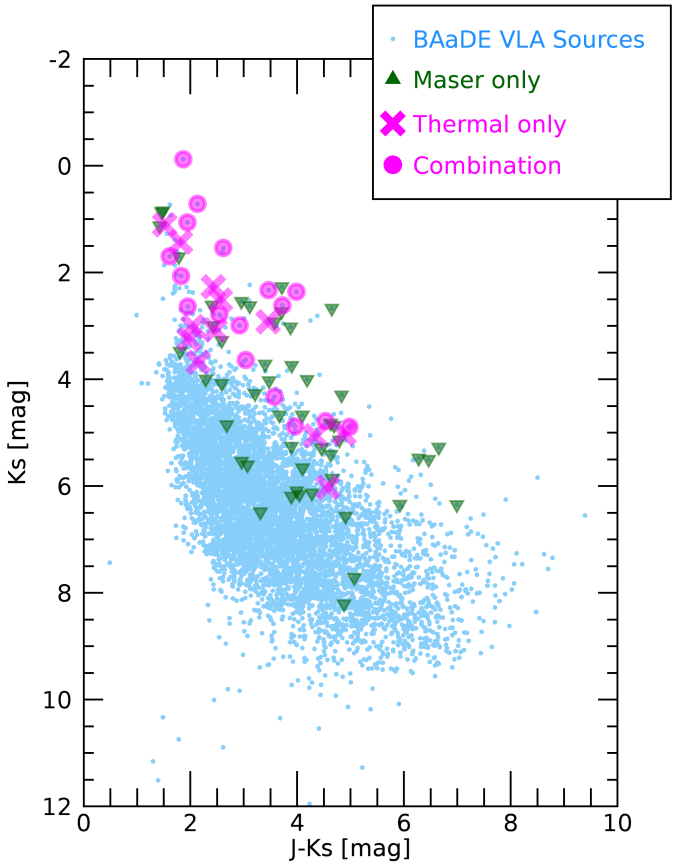

Figure 2.3: 2MASS J-Ks color against 2MASS Ks magnitude. The maser emission can be seen in sources with dimmer Ks magnitude than the thermal sources. This is likely a simple selection effect because the maser emission in our sample is typically brighter than the thermal emission.

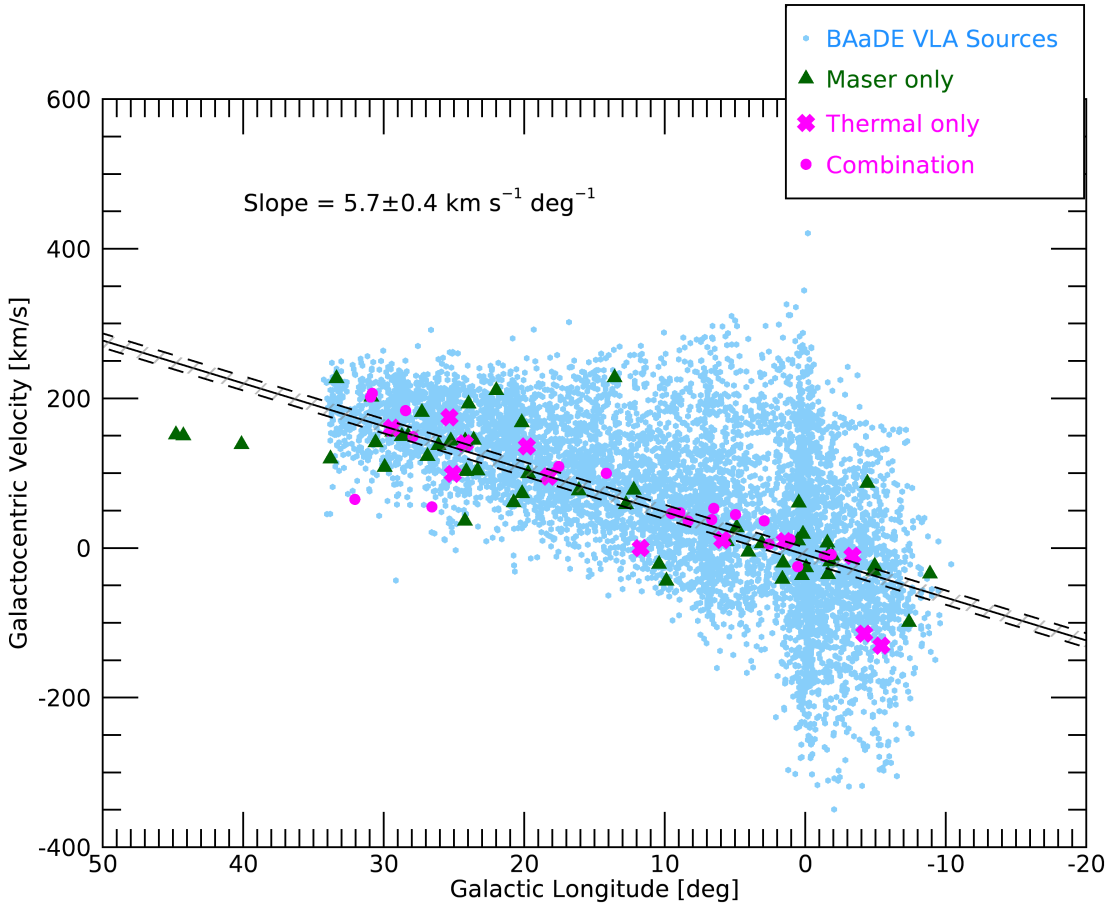

Figure 2.4: Velocity distribution with longitude of our maser and thermal sources with the BAaDE VLA survey sample for reference. The line is fit only to the ground-state maser and thermal sources that we analyze in this work, excluding an outlying maser farther than 50° from the Galactic center. The slope of the line describes the collective kinematics of our ground-state emission population.

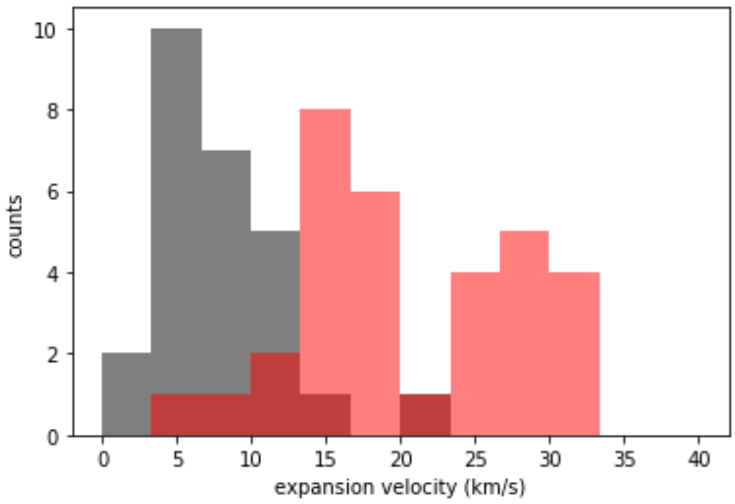

Figure 2.5: Histogram of the expansion velocity found in the previous studies of de Vicente et al. (2016) and Jewell et al. (1991) (gray) and this survey (red). We find more high-velocity outflows in our sample.

with thermal components. The four sources that we have in common with Josselin et al. (1998) have expansion velocities similar to those of CO, which tentatively suggests that the thermal SiO profiles are characterized by the region that has reached terminal velocity, as are CO profiles. There could be some secondary contribution from the dust formation zone, where the winds are being accelerated, but profiles measured with integration times longer than in our survey will be required to constrain such contributions. Future high-resolution VLBI mapping of the ground-state maser position in the circumstellar envelope would shed light on the question of what outflow regime this transition is probing, and would allow for comparison to pumping models, as in Soria-Ruiz et al. (2004), for example. Future studies could also examine the time-domain features of the $v = 0$ masers. In de Vicente et al. (2016) the sources that were followed up showed variability in the maser component that was not related to the optical or infrared variability of the stellar source.

We find that our sources are brighter than the main locus of the BAaDE survey and present no clustering in space. These properties, supplemented with a kinematic argument and some

Gaia distances, suggest that our sources are members of the disk of the Milky Way. This analysis suggests that we are seeing ground-state emission in nearby sources because it is too faint to see at greater distances, implying that deeper observations of more distant SiO sources will likely result in more detections of ground-state emission.

2.6 Appendix

Figures 2.6, 2.7, 2.8, and 2.9 contain spectra of the maser, thermal only, and composite emission sources.

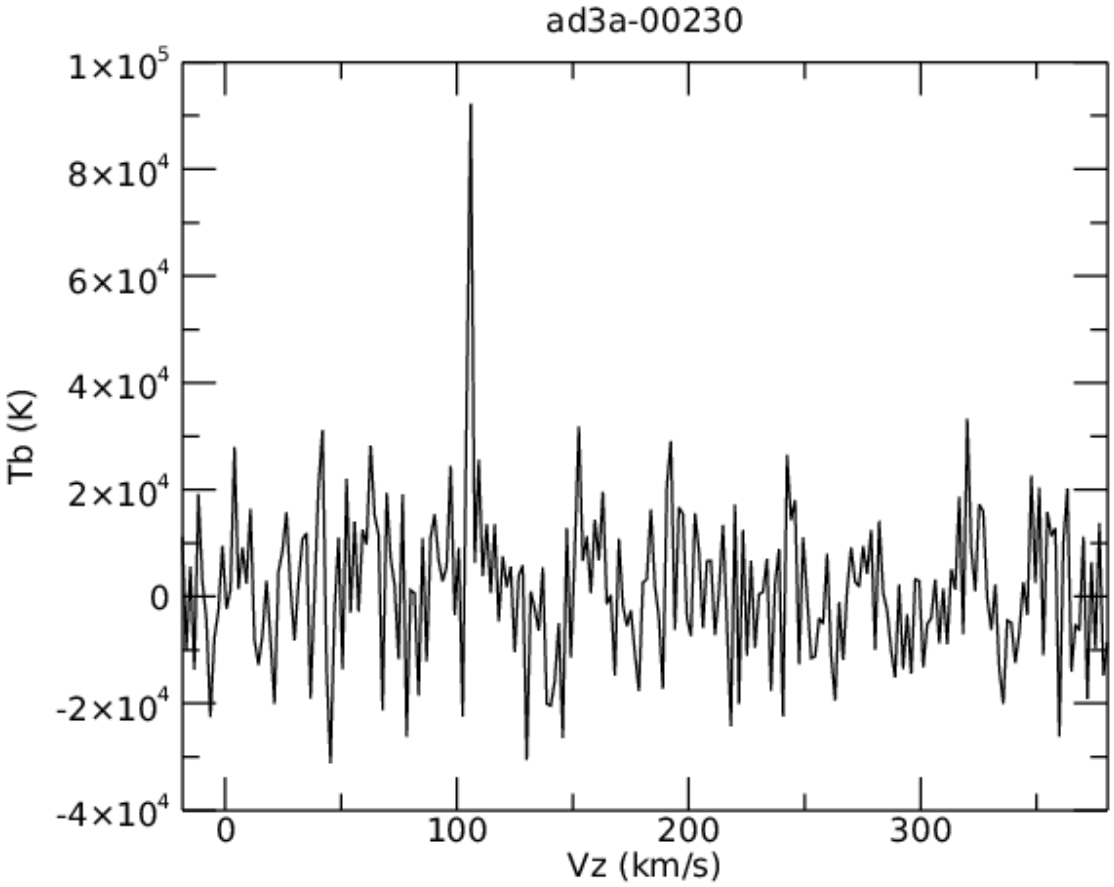

Figure 2.6: Example profile of the $v = 0, J = 1 - 0$ maser line in source ad3a-00230. V_z is the local standard of rest velocity. The complete figure set (58 maser-only spectra) is available in the online materials for the previously published version of this paper, Dike et al. (2021).

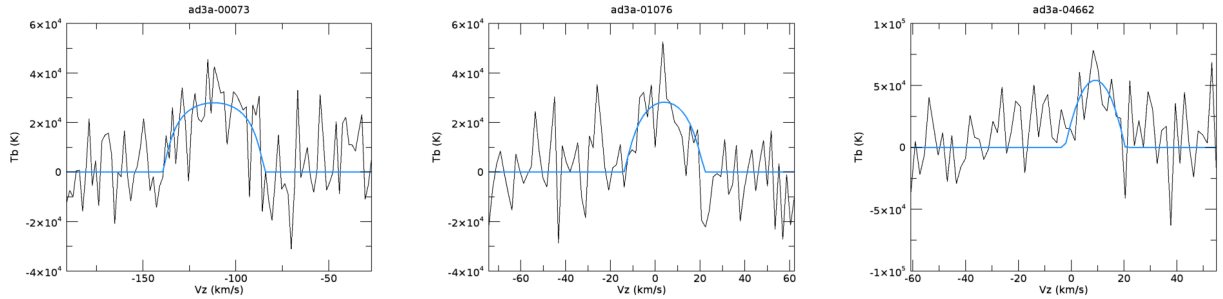

(a)

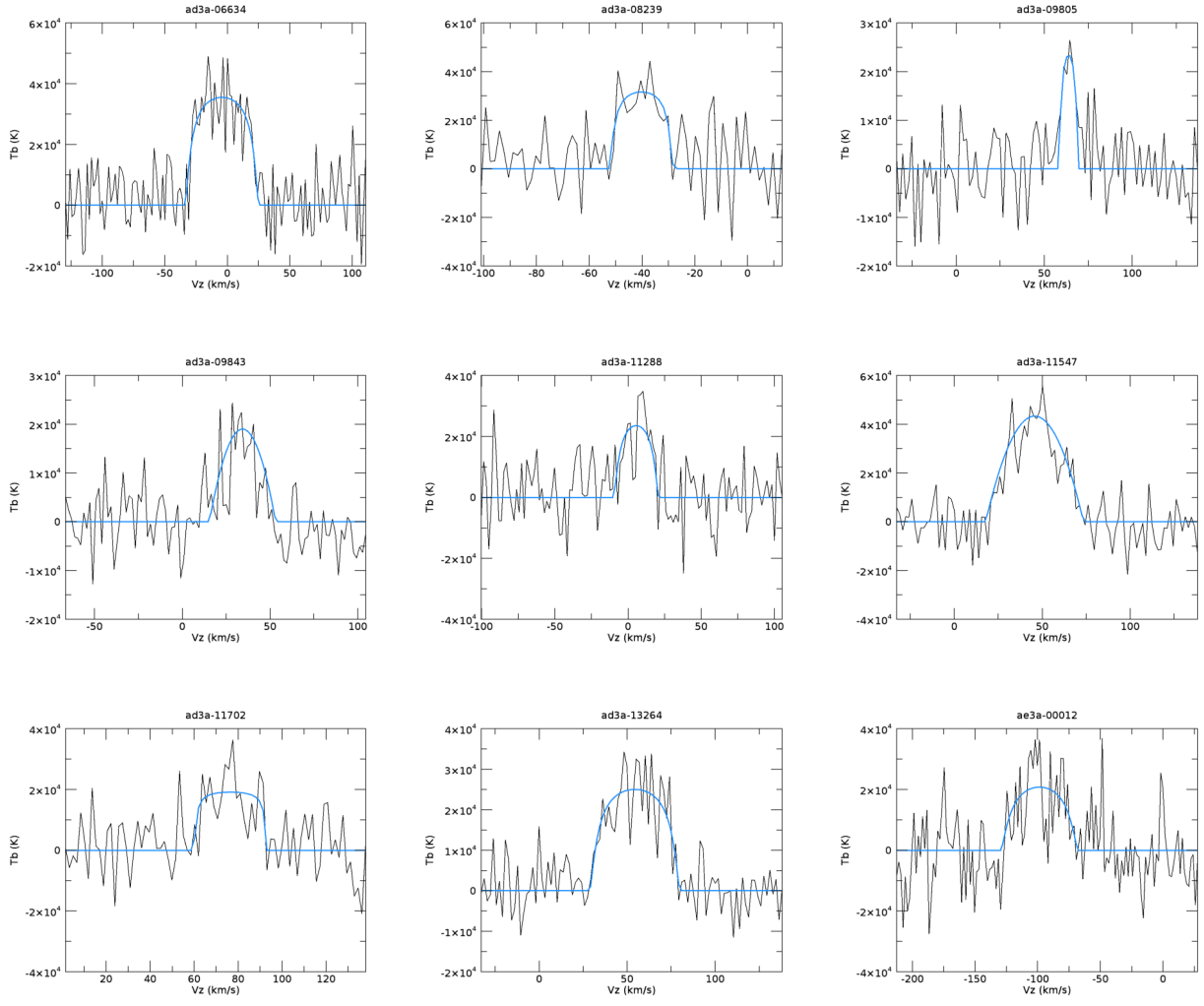

Figure 2.7: Line profiles of the thermal sources that underwent the fitting process, with the blue line indicating the model fit.

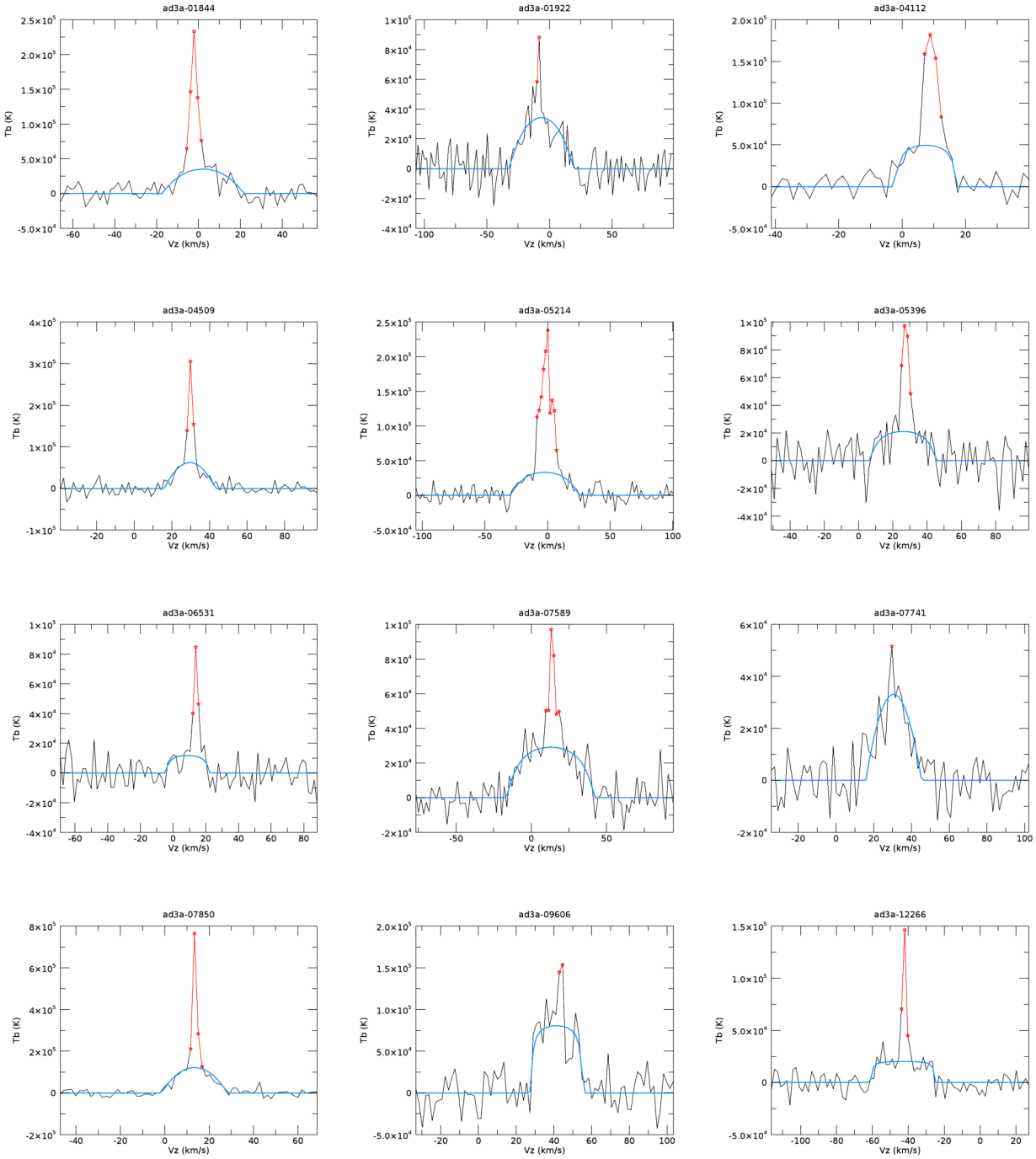

Figure 2.8: Line profiles of thermal sources with a maser component along with our model fit (overplotted blue line). Maser components were zero-weighted for the fit. The zero-weighted points are marked by red stars in these diagrams.

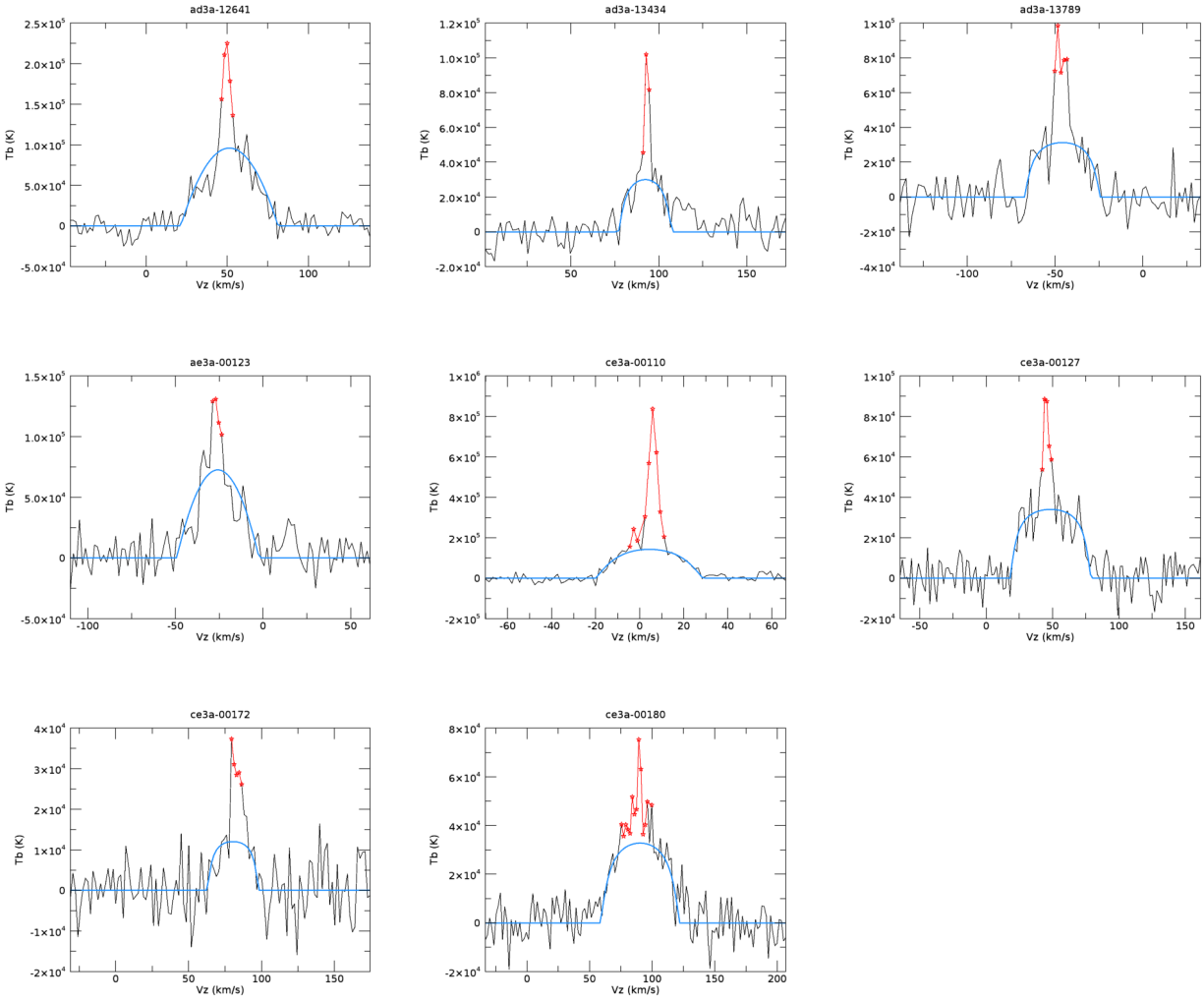

Figure 2.9: Additional combination profiles as shown in Figure 2.8.

CHAPTER 3

Strong lensing constraints on primordial black holes as a dark matter candidate

Dark matter could comprise, at least in part, primordial black holes (PBH). To test this hypothesis, we present an approach to constrain the PBH mass ($M_{\rm PBH}$) and mass fraction ($f_{\rm PBH}$) from the flux ratios of quadruply imaged quasars. Our approach uses an approximate Bayesian computation (ABC) forward modeling technique to directly sample the posterior distribution of $M_{\rm PBH}$ and $f_{\rm PBH}$, while marginalizing over the subhalo mass function amplitude, spatial distribution, and the size of the lensed source. We apply our method to 11 quadruply-imaged quasars and derive a new constraint on the intermediate-mass area of PBH parameter space $10^4 {\rm M}_\odot < M_{\rm PBH} < 10^6 {\rm M}_\odot$. We obtain an upper limit $f_{\rm PBH} < 0.17$ (95% C.L.). This constraint is independent of all other previously published limits.

3.1 Introduction

Primordial black holes (PBH) are an appealing DM candidate because they do not require physics beyond the standard model and black holes are known to exist in nature. In the early Universe, overdensities could have created the earliest black holes (Zel'dovich & Novikov 1967; Hawking 1971), and these black holes could persist into the present day to make up part or all of the dark matter (DM) in the Universe (Carr & Hawking 1974; Chapline 1975). For a recent overview of primordial black holes as a DM candidate, see Carr & Kühnel (2020)

and Green & Kavanagh (2021). Narrowing the primordial black hole parameter space can place constraints on various models of cosmological significance because PBH formation and evolution is entwined with the history of the Universe.

The hypothetical parameter space for PBH is very wide. Their mass distribution is virtually unconstrained theoretically, and they do not necessarily have to account for the entirety of DM. Observations exclude many mass ranges for PBH representing 100% of DM, but the constraints are much weaker for a population that makes up only a fraction of DM (see, e.g., Belotsky et al. 2019; Carr et al. 2020). For black holes of mass $M_{\rm PBH}$ greater than $10^2 {\rm M}_\odot$, fast radio burst lensing constrains the fraction of dark matter in PBH, $f_{\rm PBH}$, to less than 9% (Zhou et al. 2021). PBH as all dark matter requires a population of around sub-solar mass, but is consistent with the FRB rate in the model of Kainulainen et al. (2021). A stellar-mass scale PBH distribution is detectable as microlensing in strongly lensed quasars, in cases where microlensing by stars can be suppressed (Hawkins, 2020).

Carr et al. (2019) put forward a multi-peaked PBH mass function (including a high-mass peak of 10^6 $\rm M_\odot$) that could explain a range of phenomena from cosmic infrared background excess to black hole merger rates. See also Khlopov (2010) for an overview of cosmological implications of PBH formation mechanisms. PBH non-detection can itself constrain the scale of isocurvature perturbations in cold dark matter in the early Universe (Passaglia & Sasaki, 2021). A small DM fraction of high-mass PBH could seed supermassive black holes and galaxy formation (Carr & Silk, 2018), and in turn the observed population of supermassive black holes can also be used to constrain the PBH mass function (Cai et al., 2023).

A powerful and direct way to probe the PBH contribution to dark matter is strong gravitational lensing (see, e.g., Treu 2010 and references therein). Intrinsically point masses, PBH are particularly effective deflectors. Their observational signature depends only on their mass, with the deflection angle in terms of impact parameter ξ modeled as $\alpha = 4GMc^{-2}\xi^{-1}$. The method of gravitational imaging (Koopmans, 2005; Vegetti et al., 2010; He et al.,

2022)could in principle be used to detect individual PBH of masses greater than 10^3 $M_\odot$ (Banik et al., 2019), and lensing constraints from compact radio sources can also be used to constrain high-mass PBH Zhou et al. (2022). Because constraints from lensing are completely independent of others that have been used to constrain PBH in a similar mass range, such as dynamical constraints (Carr & Sakellariadou 1999, Quinn et al. 2009, Brandt 2016), X-ray background constraints on accretion rate (Inoue & Kusenko, 2017), or Lyman-α forest enhancement constraints (Afshordi et al., 2003; Mack et al., 2007; Murgia et al., 2019), lensing provides a vital cross-check.

Anomalies in the ratios of flux between images of the same lensed source can reveal substructure in the lensing mass distribution. This technique, suggested initially by Mao & Schneider (1998), can probe structure at lower mass scales than those accessible with gravitational imaging. Such flux ratio anomaly studies rely on observations of lensed sources that are large enough to avoid being affected by stellar microlensing; see Dobler & Keeton (2006) for an analysis of the effect of source size on flux ratio analysis. Examples of such sources include radio emission in radio-loud quasars (Mao & Schneider, 1998; Metcalf & Madau, 2001; Dalal & Kochanek, 2002; Hsueh et al., 2020), mid-infrared emission from the hot dust in active galactic nuclei (AGN) (Chiba et al., 2005), and the the narrow-line region of AGN (Moustakas & Metcalf, 2003; Nierenberg et al., 2014, 2017, 2020).

Gilman et al. (2020a,b) presented an analysis framework that uses the flux ratios among images in quadruply-imaged quasars (quads) to constrain the properties of dark matter structure in strong lens systems. These techniques can be adapted to constrain a variety of dark matter models, including cold dark matter (CDM), warm dark matter (Gilman et al., 2020a), self-interacting dark matter (Gilman et al., 2022a), and fuzzy dark matter (Laroche et al., 2022), given a prescription for the halo mass function and density profiles of haloes.

In this paper, we present new constraints on the PBH parameter space by analysing the flux ratio anomalies in a sample of strongly-lensed quasars observed in the narrow-line regime

(Nierenberg et al., 2014, 2017, 2020). In Section 3.2 we explain our method of sampling the posterior distribution of our PBH parameters of interest using forward modeling. In Section 3.3, we present the results of our modeling and comparison to real data, and in Section 3.4 we discuss further expansions on this study. When necessary, we use the cosmology parameters of Planck Collaboration et al. (2020) throughout this analysis, although we stress that our results do not depend sensitively on this assumption.

3.2 Methods

In this section, we first describe the goal of this paper, to obtain a posterior distribution on the PBH parameters of interest, which we achieve using an Approximate Bayesian Computing forward modeling method. We first model the lens substructure using the method developed in Gilman et al. (2019), and then we model the effect of a possible PBH population.

3.2.1 Inference

We are striving to measure the posterior probability of dark matter model parameters; here our likelihood function $\mathcal{L}$ can be written as:

$$\mathcal{L}(D_i|\theta_{f,M}) = \int p(D_i|m_r, \theta_r) p(\theta_r, m_r|\theta_{f,M}) dm_r d\theta_r, \tag{3.1}$$

where D_i is the observed image positions and flux ratios for a certain lens, $\theta_{f,M}$ represents our target model parameters, $M_{\rm PBH}$ and $f_{\rm PBH}$, m_r is a certain lens model realization, and θ_r is the set of non-PBH model parameters that we marginalize over. We use the method described by Gilman et al. (2020a) to sidestep evaluating this integral directly, which would require a computationally intractable exploration of a vast parameter space. This sidestepping is accomplished by forward modeling data, generating flux ratios from many sets of model parameters, and then comparing the results to the observed data via a summary statistic; from this process we can extract $\theta_{f,M}$ that represent our posterior probability distribution. This

is an Approximate Bayesian Computing (ABC) method (Rubin 1984, see also, e.g., Sisson et al. 2018) of creating a large set of stochastically varying simulated data and accepting simulations close to the real data to sample a posterior. ABC has been used in astrophysical forward-modeling problems where a direct calculation of the likelihood function is infeasible and data can be simulated; see, e.g., Weyant et al. (2013), Akeret et al. (2015), Birrer et al. (2017).

We use the sample of eleven quadruply-imaged quasars selected for flux ratio analysis by Gilman et al. (2022b, Section 2.2) because the size of the source, either observed as O[III] emission from the narrow line region or CO (10-11) radio emission, is larger than the scale that would be affected by microlensing or image arrival time delay, and the main lensing galaxy does not require modeling for a known stellar disk component (Hsueh et al. 2016, Hsueh et al. 2017, Gilman et al. 2017). Photometry data used for each lens is referenced in Table 3.1.

We generate a lens model using lenstronomy[1] (Birrer & Amara, 2018; Birrer et al., 2021). The lens model is optimized to match the observed image position, with the added astrometric uncertainty. Any draw of parameters that does not match the observed image positions would be rejected in the posterior, so we reduce computation time by requiring the lens model fit the positions.

We compute the magnification, and thus the flux, of each image in our lens system model realization, then obtain the three flux ratios $r_{\rm model}$ between the four images. Only flux ratios are used because the intrinsic source brightness is not known. We compare the forward-modeled flux ratios to the observed flux ratios $r_{\rm obs}$ with the summary statistic

$$S(r_{\rm model}, r_{\rm obs}) = \sqrt{\sum_{\rm i=1}^{3} (r_{\rm model(i)} - r_{\rm obs(i)})^2}. \tag{3.2}$$

[1] https://github.com/sibirrer/lenstronomy

We generate $\mathcal{O}10^5$ - 10^6 lens model realizations sampling from our parameter space from which we choose the 1,500 lowest summary statistics to represent a sample of the posterior distribution. We construct a continous approximation of the likelihood function for each lens by applying a kernel density estimate to the accepted samples, and multiply the resulting likelihoods to obtain the final posterior.

3.2.2 Model parameters

The lens and halo substructure modeling process follows from Gilman et al. (2020b), Gilman et al. (2020a), and Gilman et al. (2019). The lensing galaxy, or main deflector, is modeled as a power-law ellipsoid with external shear. The properties of the main deflector that are optimized during initial lens model fitting are the Einstein radius, centroid, ellipticity, ellipticity angle, and shear angle. If the main deflector has any known satellite galaxies, they are included in the model as a singular isothermal sphere mass profile. The main deflector mass $M_{\rm host}$, log profile slope $\gamma_{\rm macro}$, and shear $\gamma_{\rm ext}$ are sampled in the forward model.

Subhaloes are rendered from 10^6-10^{10}M$_\odot$, from the lowest mass we are sensitive to to the highest mass of halo we expect to be entirely DM. The projected mass density $\sum_{\rm sub}$ and power-law slope α parameterize the subhalo mass function (SHMF),

$$\frac{d^2N_{\rm sub}}{dmdA} = \frac{\Sigma_{\rm sub}}{m_0}\left(\frac{m}{m_0}\right)^{\alpha}\mathcal{F}(M_{\rm halo}, z), \tag{3.3}$$

where $\mathcal{F}(M_{\rm halo}, z)$ is a function to scale the number density of subhaloes with main lensing halo mass and redshift as described in Gilman et al. (2020a). The pivot mass m_0 is set to 10^8M$_\odot$ (Fiacconi et al., 2016). For the line-of-sight haloes, we use the Sheth-Torman halo mass function (Sheth et al., 2001a) with two-halo term $\xi_{\rm 2halo}$ as a scaling factor to account for correlated structure near the host halo (see Gilman et al. 2019) and $\delta_{\rm los}$ as an overall amplitude scaling factor:

$$\frac{d^2N_{\rm los}}{dmdV} = \delta_{\rm los}(1+\xi_{\rm 2halo}(M_{\rm halo}, z))\frac{d^2N}{dmdV}|_{\rm ShethTormen}. \tag{3.4}$$

Given the PBH mass is distributed along with CDM subhaloes, the Sheth-Torman mass

function should be broadly applicable, but there may be an enhancement of the power spectrum on small scales caused by isocurvature perturbations from PBH (Afshordi et al., 2003; Gong & Kitajima, 2017). Our constraint is more conservative because we do not take this enhancement into account. The free model parameters and priors are as follows:

- $M_{\rm PBH}$ [$M_\odot$], the PBH monochromatic mass, with a prior of 10^4-$10^6 M_\odot$ chosen to include PBH that are large enough to affect the flux ratios given the background source size but not larger than the minimum rendered halo mass;

- $f_{\rm PBH}$, the PBH mass fraction of total DM, with a prior of 0-50%;

- $\Sigma_{\rm sub}$, the SHMF normalization, with a prior of 0-0.1 kpc^{-2}. We allow broad uncertainty in the number of subhaloes to account for uncertainties associated with tidal stripping;

- α, the log slope of SHMF, with a prior ranging from -1.85 to -1.95 as predicted by ΛCDM N-body simulations (Springel et al. 2008, Fiacconi et al. 2016);

- $\delta_{\rm los}$, the line-of-sight halo mass function scaling factor, with a prior of 0.8-1.2 that accounts for differences between theoretical models of the halo mass function (e.g. Despali et al., 2016) and uncertainties in cosmological parameters;

- $\gamma_{\rm macro}$, the log slope of main deflector mass profile, with a data-motivated prior of 1.9-2.2 (Auger et al. 2010);

- $\sigma_{\rm source}$, the background source size, differing depending on whether the source is observed in narrow-line (Müller-Sánchez et al., 2011) or other regions (Chiba et al., 2005; Stacey et al., 2020) surrounding the background quasar listed for each lens in Table 3.1 ;

- $M_{\rm host}$, the mass of the main lens host galaxy (see Table 3.1 and Gilman et al. (2020a) for a discussion of these priors constructed from individual lens data);

- $\gamma_{\rm ext}$, the external shear in the main lens plane (see Table 3.1, with ranges based on the individual lens data determined in Gilman et al. (2022b));
- $\delta_{\rm xy}$ [milliarcsec], the image position uncertainty;
- $\delta_{\rm f}$, the image flux uncertainty.

References to photometric measurement information are listed in Table 3.1. Our target parameters are $M_{\rm PBH}$ and $f_{\rm PBH}$, and we marginalize over the others when they are sampled together in the posterior. For each realization, the model parameters are drawn from a prior distribution and the halo placement is stochastic. Some lenses have photometrically-estimated redshifts (Gilman et al., 2020a) so we sample the redshift probability distribution function and marginalize over it for those lenses.

Lens RXJ1131+1231 was modeled with two Gaussian source components to match the data of Sugai et al. (2007). Lenses with an imaged satellite companion are modeled with the companion in the source plane as a single isothermal sphere with position uncertainty of 50 milliarcsec.

3.2.3 PBH deflection modeling

If some fraction $f_{\rm PBH}$ of dark matter exists in the form primordial black holes, the distribution of these objects should follow a population of haloes with Navarro-Frenk-White (NFW) profiles (Navarro et al., 1997). Thus, the first step in our analysis is to generate a population of NFW haloes and subhaloes throughout the lensing volume. We create a realization of DM haloes and subhaloes using the lenstronomy affiliate package pyHalo[2] (Gilman et al., 2021). We can calculate the mass fraction of dark matter rendered in haloes $f_{\rm halo}$, which we use to determine the number of PBH that is clustered with the halo mass, and a stochastic distribution of line-of-sight and lens-plane subhalo masses, which we use to determine the

[2] https://github.com/dangilman/pyHalo

Table 3.1: Priors for the parameters in our model that are lens-dependent. For a description of all free parameters, including those with priors shared between all lenses, see text. The host halo mass $M_{\rm host}$ has a Gaussian prior and other priors are uniformly distributed. The rightmost column has the reference for the photometry data.

Lens Name	σ_{source} [pc]	M_{host} [$M_\odot$] (μ, σ)	γ_{ext}	Ref.
B1422+231	25-60	13.3, 0.3	0.08-0.4	*a*
HE0435-1223	25-60	13.2, 0.3	0.015-0.15	*b*
MG0414+0513	5-15	13.5, 0.3	0.01-0.32	*c d*
PG 1115+080	5-10	13.0, 0.3	0.002-0.12	*e*
PS J1606-2333	25-60	13.3, 0.3	0.1-0.28	*f*
RX J0911+0551	25-60	13.1, 0.3	0.05-0.25	*f*
RX J1131-1231	25-80	13.9, 0.3	0.06-0.28	*g*
WFI 2026-4536	25-60	13.3, 0.3	0.015-0.16	*f*
WFI 2033-4723	25-60	13.3, 0.3	0.07-0.26	*f*
WGD J0405-3308	25-60	13.3, 0.3	0.0025-0.12	*f*
WGD 2038-4008	25-60	13.04, 0.15*	0.005-0.08	*f*

*This value from Shajib et al. (2022)

References — [a]Nierenberg et al. (2014) [b]Nierenberg et al. (2017) [c]Stacey & McKean (2018) [d]Stacey et al. (2020) [e]Chiba et al. (2005) [f]Nierenberg et al. (2020) [g]Sugai et al. (2007)

clustered PBH position.

To determine the spatial distributiion of the black holes at each redshift plane along the line of sight, we first compute the projected mass in dark matter at the lens plane from the population of NFW haloes distributed throughout the lensing volume. If we were to render haloes down to the minimum halo mass in CDM, then all of the PBH would track the density of dark matter in haloes. However, as we only render a fraction of the total mass of dark matter in haloes, a number $N_{\rm clustered} = (f_{\rm PBH})(f_{\rm halo})(\rho_{\rm DM}(z))(V/M_{\rm PBH})$ will track the dark matter density in haloes. We distribute this population of PBH with a spatial probability density that varies in proportion with the project mass in dark matter at each lens plane, as illustrated by Fig. 3.1. The mass added in PBH is removed from the rendered particle-DM subhalo mass. We place the remaining $N_{\rm smooth}$ point masses randomly across each redshift plane, tracking the smooth background distribution of dark matter that we do not place in haloes. For each image of the lens, we add PBH at discrete redshift steps along the line of sight within a circular aperture of 0.24" for 10^8 $M_\odot$, scaling with the root $M_{\rm PBH}$ to a minimum of 0.15". For images closer than 0.24", we add half the distance between the two points to the aperture and centre it at the midpoint between the images, treating the rendering area for those images as one aperture as illustrated in Fig. 3.2.

In Fig. 3.3 we have plotted effective multiplane convergence for a lens model with $M_{\rm PBH} = 10^{5.5}{\rm M}_\odot$ and $f_{\rm PBH} = 0.4$ alongside that of a model with no PBH substructure. This effective multplane convergence is defined as the multiplane convergence (half the divergence of the effective deflection through the lensing planes $\boldsymbol{\alpha}_{\rm eff}$) from the lens model minus the macro-model convergence, thus $\kappa_{\rm eff} \equiv \frac{1}{2}\nabla \cdot \boldsymbol{\alpha}_{\rm eff} - \kappa_{\rm macro}$. On a convergence map, which corresponds to surface density, the point masses produce markedly different lensing signatures to the less centrally concentrated NFW profiles.

After the PBH have been distributed in the lens model, the deflection from the new point masses is accounted for by re-fitting the lens model to the observed image positions. We

raytrace through this final lens model to get the simulated image flux ratios, and calculate our summary statistic for the realization.

3.3 Results and comparison with previous work

We present our constraint on PBH dark matter from the posterior distribution of our target PBH parameters for 11 lenses in (Fig. 3.4), which were combined and marginalized over the main deflector and subhalo parameters described in Section 3.2.2. We obtained a 95% upper limit on $f_{\rm PBH}$ of 0.17 accross the probed mass range. We see there is a tentative anticorrelation between $M_{\rm PBH}$ and $f_{\rm PBH}$, as we would expect.

Our constraint is plotted along with others in the same mass range in Fig. 3.5. The constraint is stronger than that placed by radial velocity measurements of three wide binary systems that could be disrupted by a PBH population (Quinn et al., 2009), but it is partially within the bounds of the other four constraints. However, our method is totally independent of the other bounds, and thus provides an important cross-check of the assumptions of other methods, and their potential systematic uncertainties.

The X-ray accretion background constraint depends sensitively on assumption about the physics of gas accretion on to PBH and the possible subsequent formation of an accretion disk, the density of the interstellar medium (ISM), and PBH motion through the ISM. The constraint shown from Brandt (2016), similar to that of Quinn et al. (2009), is from the survival of the Eridanus II star cluster that would be dynamically heated into dispersal by PBH dark matter. This assumes that the Eridanus II cluster formed in place. The dynamical constraint placed by Carr & Sakellariadou (1999) assumes that PBH will drift to the centres of galaxies, but this has been argued to be avoidable if PBH are regularly dynamically ejected as well (Xu & Ostriker, 1994). The large-scale structure constraint in Figure 3.5 is from the effect of PBH on the matter power spectrum as probed by the Lyman-α forest, which in turn depends on assumptions and modeling of its thermodynamics (Villasenor et al., 2022;

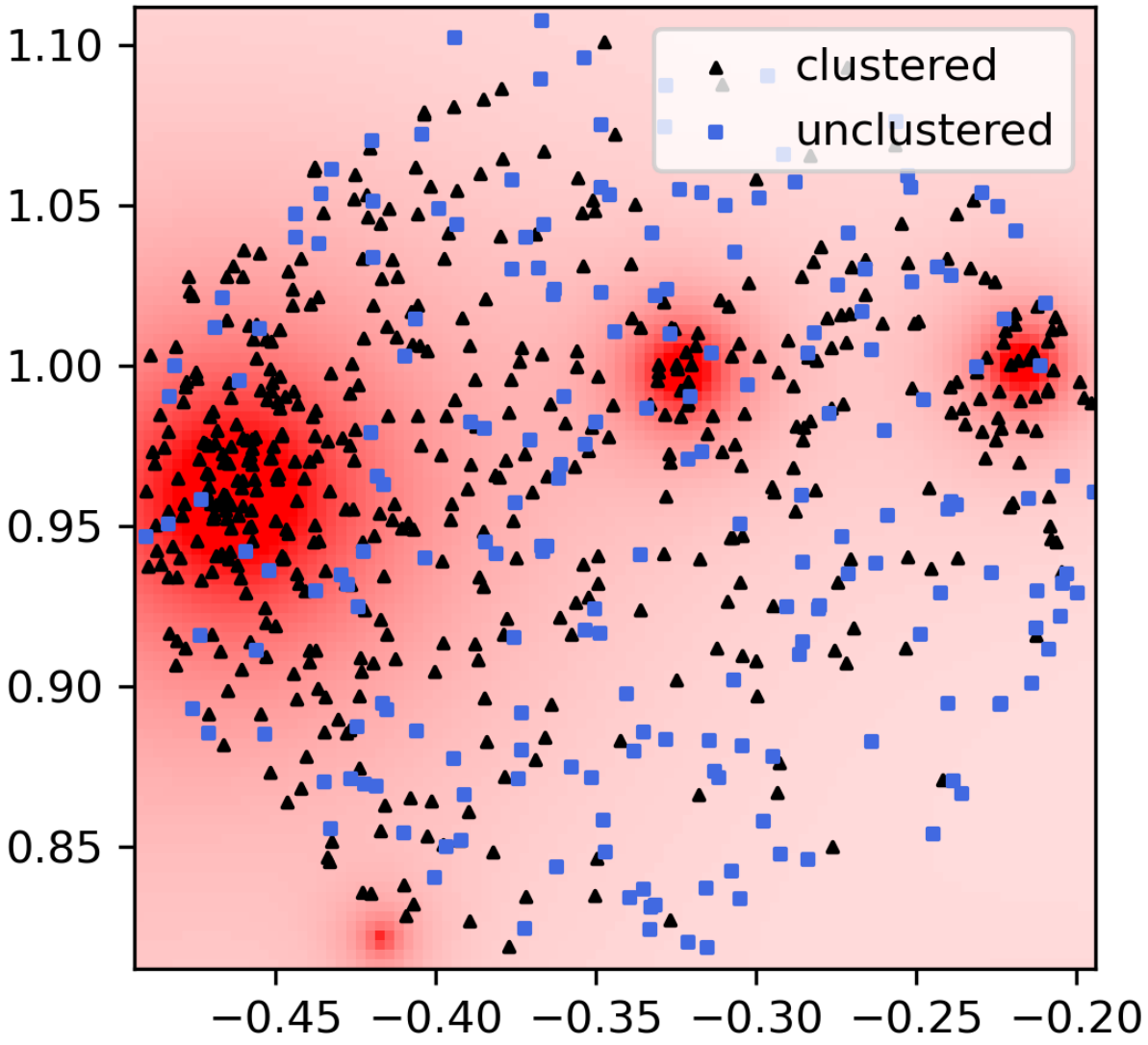

Figure 3.1: An example of PBH positions in a single lens plane. In this figure, $M_{\rm PBH}$ is 10^4 $M_\odot$ and $f_{\rm PBH}$ is 0.5. The axes are in arcseconds and the background colormap intensity varies linearly with the projected mass in dark matter. The unclustered population (blue squares) is distributed uniformly across the rendering aperture, while the clustered population (black triangles) tracks the projected dark matter mass density in haloes.

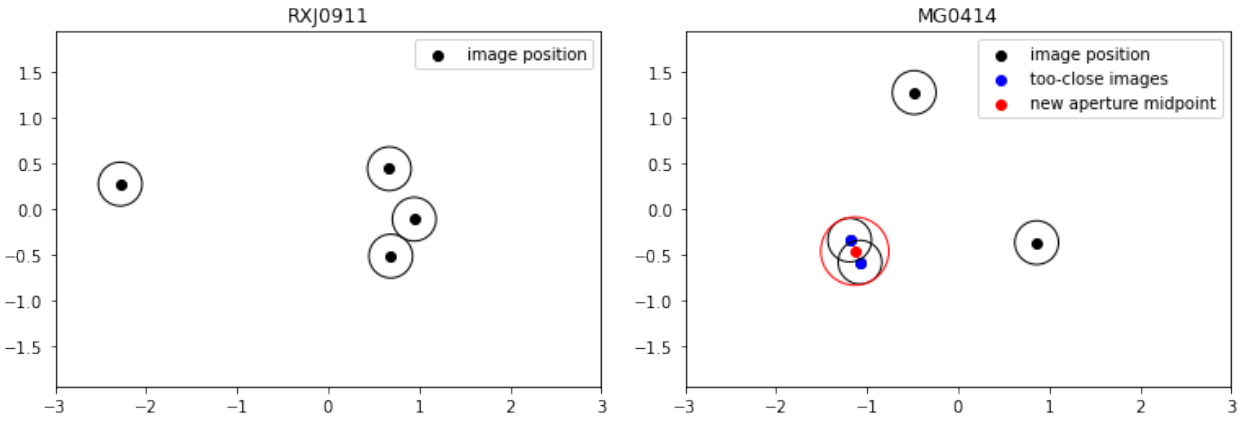

Figure 3.2: Visualization of rendering area relative to image position. The circles around the image positions represent the rendering area for lensing substructure. On the left, for lens RX J0911+0551, these areas do not overlap for the chosen radius of 0.24". On the right, there is significant overlap between the rendering areas for two images, so a new aperture is drawn around both images to avoid double-placement of PBH in the overlap region.

Viel et al., 2013).

Finally, as shown by Banik & Bovy (2021), N-body simulations with dark matter particle masses comparable to the PBH mass range we consider result in small-scale perturbations to stellar streams. Interpreting this result in the context of primordial black holes suggests streams also can constrain the contribution of PBH to the dark matter.

3.4 Discussion and conclusions

We develop a new method for including PBH substructure in a lens model for flux ratio analysis, and present independent constraints on the fraction of dark matter that could be composed of relatively massive primordial black holes. We obtained a constraint on $f_{\rm PBH}$ less than 0.17 for $M_{\rm PBH} = 10^4$-$10^6 {\rm M}_\odot$ (95% C.L.). The mass distribution for the PBH in this work is monochromatic as a conservative constraint, but the limit can be converted to an arbitrary extended mass distribution via the method presented in Carr et al. (2017). This

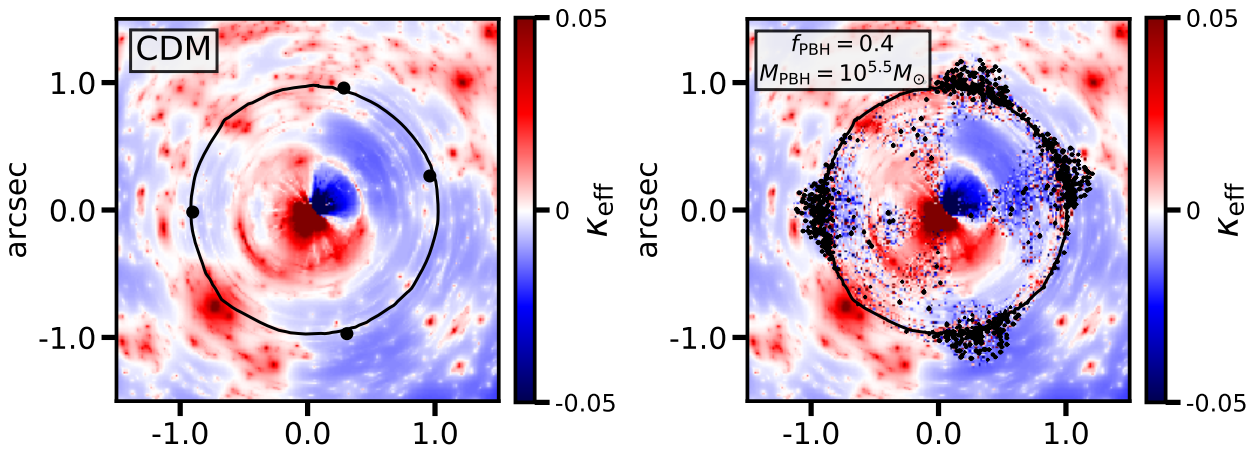

Figure 3.3: Effective multiplane convergence, a two-dimensional representation of a full population of line of sight haloes and subhaloes, for a dark matter realization in CDM (left) and with PBH substructure (right). Red corresponds to a density higher to that of the mean dark matter density, while blue corresponds to an underdensity. Black circles are plotted at each of the four quad image positions, and the black curves are the critical curves, which follows the region of maximum image magnification. Small-scale features in the convergence map that appear to track towards the origin are associated with black holes rendered around the path followed by the lensed light rays. Deformation of the critical curve by the PBH population suggests they will strongly perturb image flux ratios.

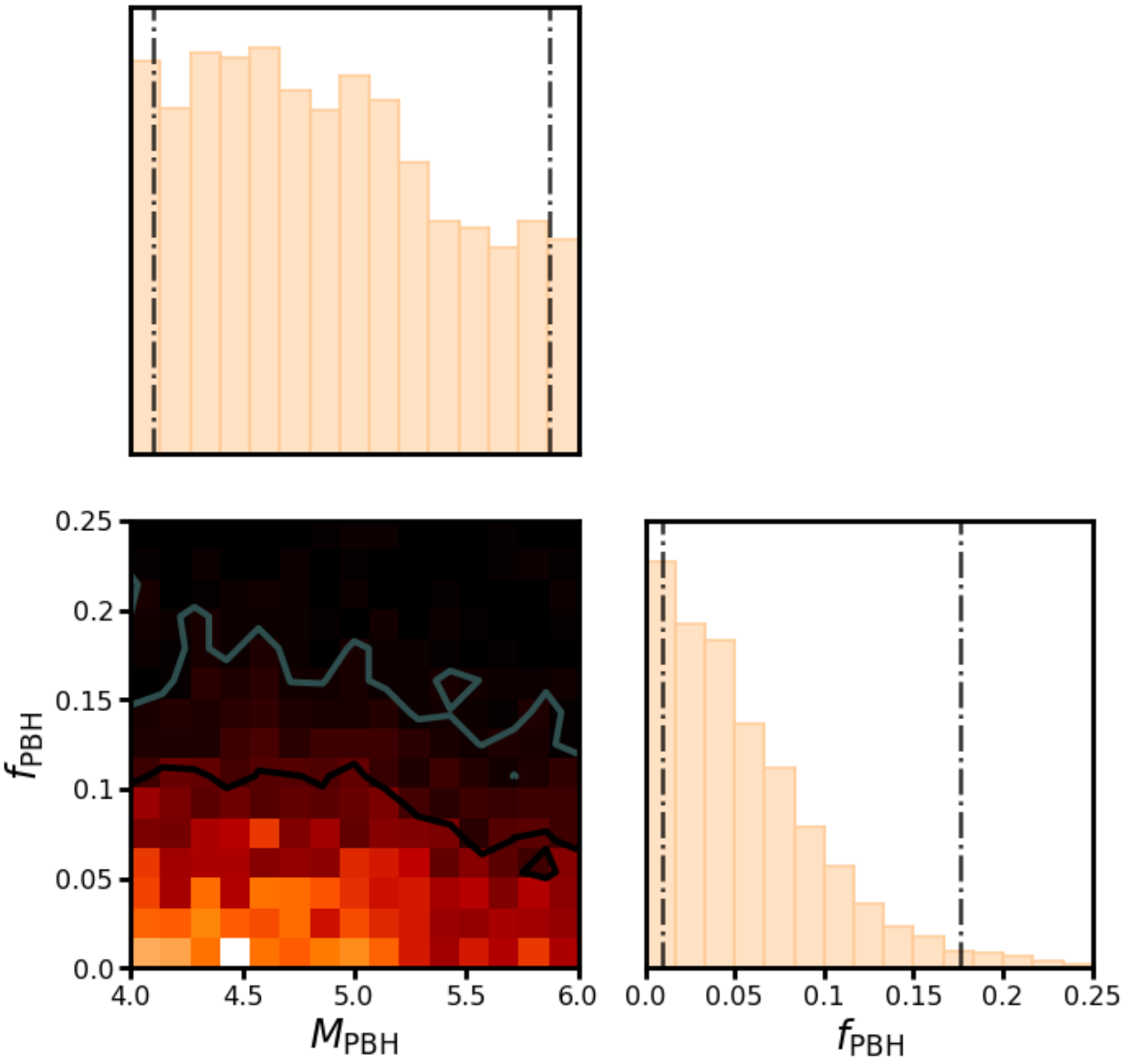

Figure 3.4: Joint posterior distribution of the PBH mass and mass fraction obtained from analyzing eleven strong lenses, marginalized over $\Sigma_{\rm sub}$, α, and $\delta_{\rm los}$. The vertical dot-dash lines in the panels showning marginal likelihoods represent 95% confidence intervals. The lighter contours are 95% confidence region and the darker contours bound the 68% confidence region.

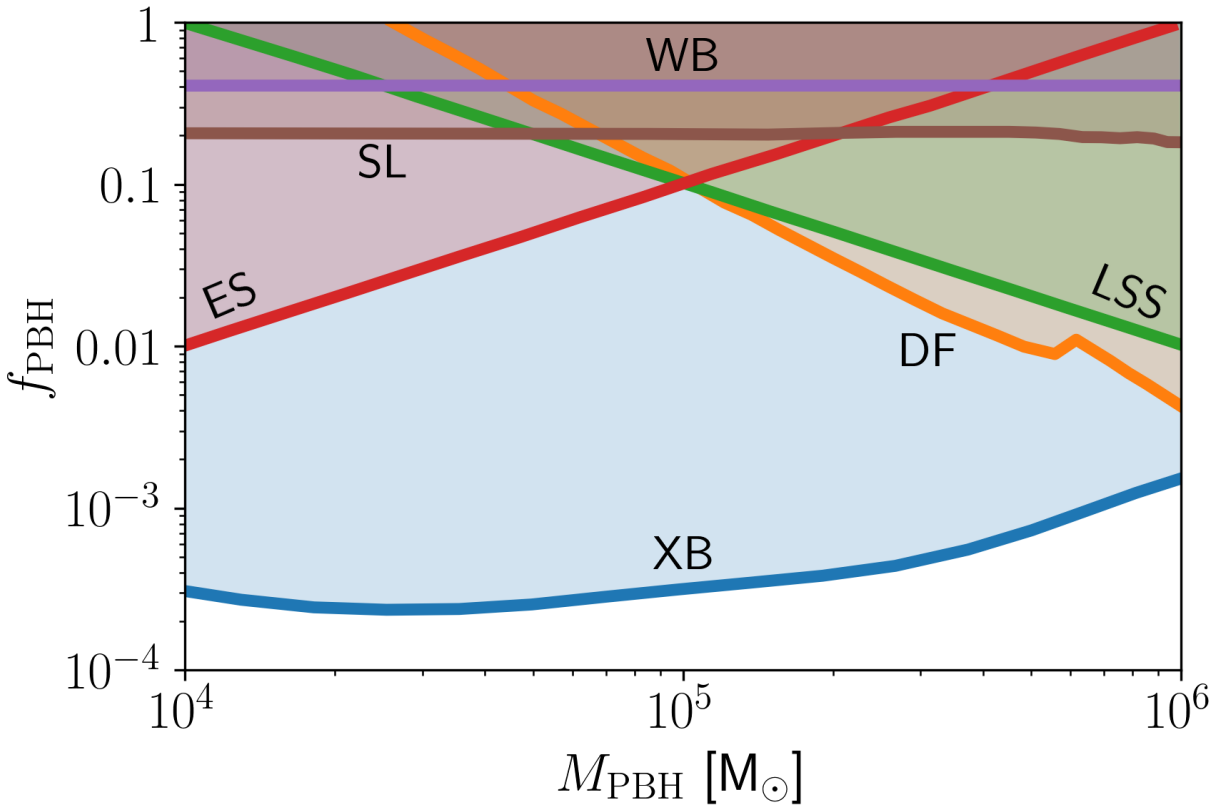

Figure 3.5: Constraints from disruption of wide binaries (WB) (Quinn et al., 2009), Eridanus II star cluster surviving possible destruction by dynamical heating (ES) (Brandt, 2016), halo dynamical friction (DF) (Carr & Sakellariadou, 1999), large-scale structure (LSS) (Afshordi et al. 2003, Mack et al. 2007), X-ray background from accretion (XB) (Inoue & Kusenko, 2017), and our constraint from strong lensing flux ratio analysis (SL).

constraint is totally independent of others in the same mass range.

In the spirit of a first application of this method, we make several simplifying assumptions throughout this process. We do not account for the effect of PBH formation on the assembly history of subhaloes and how that could possibly affect the mass functions and density profiles that we are also assuming. We allow for a very general parameterized form of these functions and marginalize over the parameter space to reduce the rigidity of our models. As samples of quads improve and our method becomes more constraining, we will revisit the simplifying assumptions.

In the future, these constraints will be improved by applying the method to larger samples of lenses that are currently being discovered (Schmidt et al., 2022) and will be discovered in wide field surveys such as the Vera C. Rubin, Euclid, and Roman Observatories (e.g. Oguri & Marshall, 2010). Lens systems can also be followed-up with adaptive optics assisted instruments from the ground (Wright et al., 2019; Wizinowich et al., 2022). Forthcoming data from the *James Webb Space Telescope (JWST)* (Nierenberg et al., 2021) will allow us to push to lower PBH mass scales because *JWST* will measure flux ratios in the mid-infrared. This emission comes from a more spatially compact ($\sim 1-10$ pc) region around the background source. The minimum deflection angle that impacts our data is determined by the size of the source, so the more compact source size will allow us to push to lower PBH mass scales than we can currently measure.

3.5 Appendix: Testing the Pipeline

Using 50,000 simulated lens model realizations of B1422+231, we tested the performance of our method by applying it to simulated data. We choose a realization with a low target mass and mass fraction of PBH and used the simulated flux ratios as the "true" flux ratios in the computation of the summary statistic. From this, we obtain the posterior distributions shown in Fig. 3.6. We repeat the exercise using a high PBH mass and mass fraction, and

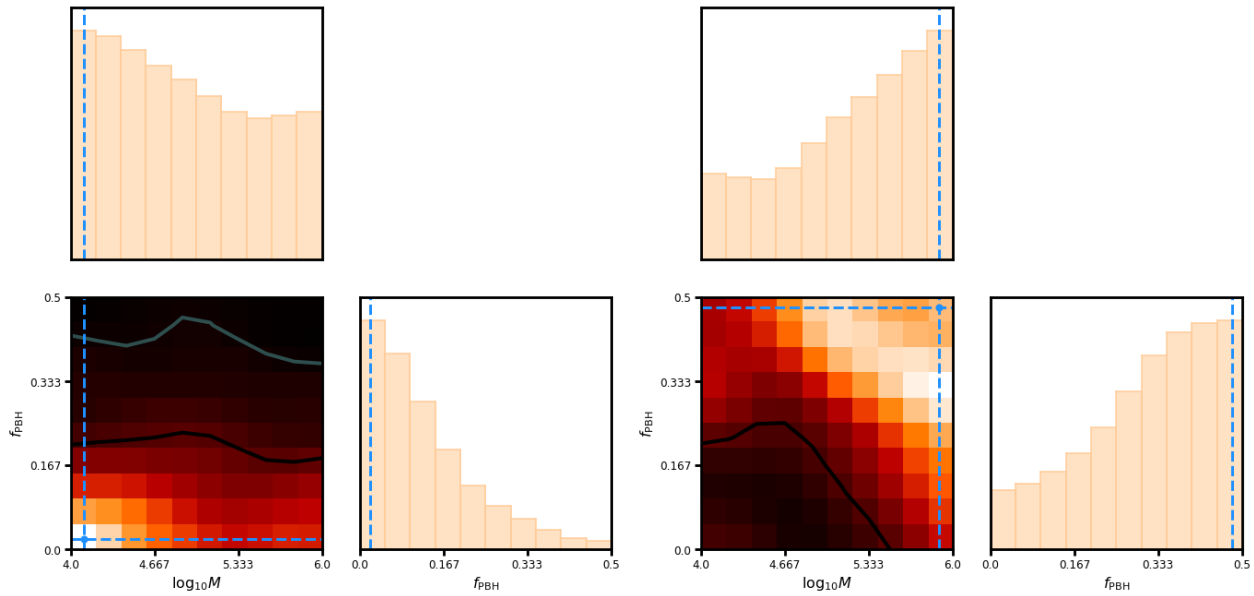

Figure 3.6: Posterior distributions created from simulated data using image positions and lensing priors of B1422+231. The posteriors are drawn from the 250 closest samples to the simulated "truth" flux ratios represented by dashed blue lines and corresponding to $M_{\rm PBH} = 10^{4.1}{\rm M}_\odot$, $f_{\rm PBH} = 0.02$ on the left and $M_{\rm PBH} = 10^{5.9}{\rm M}_\odot$, $f_{\rm PBH} = 0.48$ on the right.

show the resulting inference on the right of Fig. 3.6. The other parameters described in Section 3.2 were fixed in the middle of their uniform prior ranges. This process was carried out similarly for the lenses PS J1606-2333 and WGD J2038-4008, and the marginalized joint posterior distribution of all three lenses is shown in Fig. 3.7.

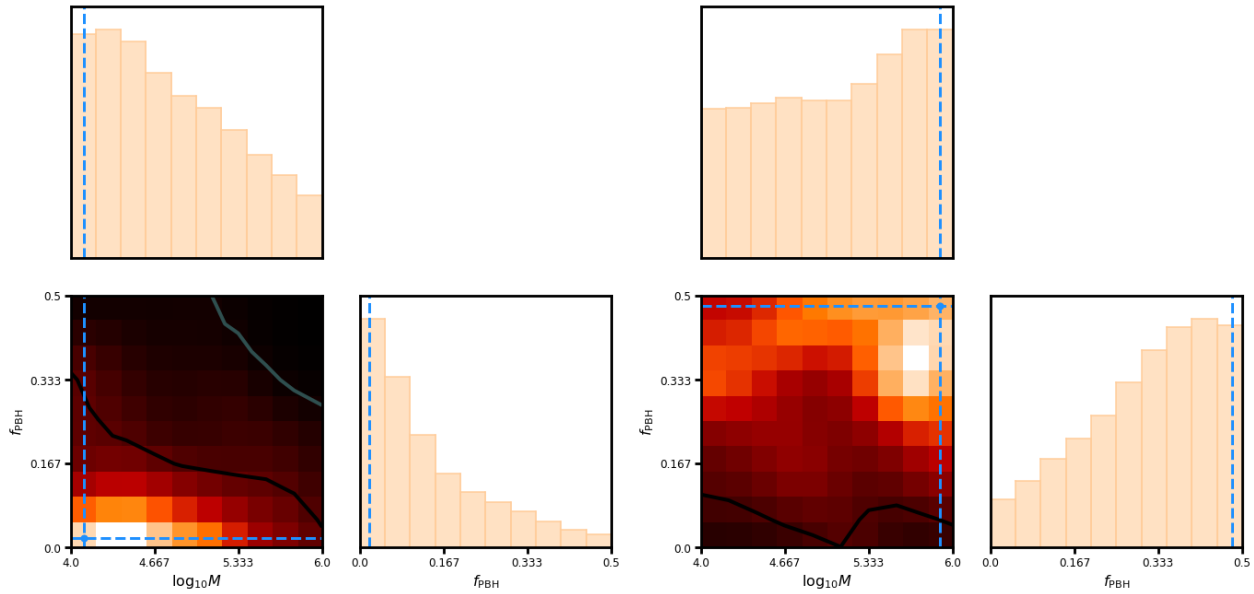

Figure 3.7: Product of posterior distributions based on image positions and priors of the three lenses B1422+231, PS J1606-2333, and WGD J2038-4008. As in Fig. 3.6, the selected "true" flux ratios used to obtain each distribution are $M_{\rm PBH} = 10^{4.1}{\rm M}_{\odot}$, $f_{\rm PBH} = 0.02$ on the left and $M_{\rm PBH} = 10^{5.9}{\rm M}_{\odot}$, $f_{\rm PBH} = 0.48$ on the right.

CHAPTER 4

Strengthening limits on intermediate-mass primordial black hole dark matter fraction

We update the primordial black hole (PBH) limits placed by our strong lensing flux-ratio analysis method. First, we describe how we will use mid-infrared JWST observations of the lensed torus of quadruply-imaged quasars to expand the sample of lenses available for use of this method, and to combine these new flux-ratio measurements with previous measurements in optical, mid-infrared, and radio to strengthen the constraining power of those lenses with multiple measurements. Finally, we combine the flux-ratio limit with other limits from independent probes in the same mass sensitivity range of 10^4-10^6 $M_\odot$ to provide a comprehensive combined limit for intermediate-mass PBH.

4.1 Introduction

Primordial black holes (PBH) are the predicted result of the phenomenon of collapse of an overdense region in the radiation-dominated Universe after inflation (Zel'dovich & Novikov 1967, Hawking 1971; see also Sasaki et al. 2018). Low-mass PBH could make up all of dark matter, or a population of PBH at any mass could make up a significant fraction of dark matter (see reviews in Carr & Kühnel 2020, Green & Kavanagh 2021, and Carr et al. 2023). An intermediate-mass population of PBH could be useful for explaining the seeding of supermassive black holes in galaxies (Carr et al., 2019). Strong lensing is sensitive PBH

at this mass, and a 95% confidence limit was placed on the fraction of PBH $f_{\rm PBH} < 0.17$ within the mass range $M_{\rm PBH} = 10^4$-10^6 $M_\odot$ using a flux-ratio analysis of quadruply imaged quasars (quads) in Dike et al. (2023).

The limits provided by a strong lensing flux-ratio analysis can be improved with an increase in the the total number of lenses (with a factor of improvement proportional to the square root of the number of lenses), an increase in measurements used for each lens, as well as an improvement in the precision of photometry of those measurements (see Gilman et al. 2019). In this paper, we update the limits of Dike et al. (2023). In section 4.2, we review the flux-ratio analysis method used to obtain the constraint. In section 4.3, we describe the three ways we update the constraint: through increasing the sample size with JWST lensing observations (Nierenberg et al., 2021), incorporating new JWST flux ratio measurements with those used previously at other wavelengths for the original sample of eleven lenses, and finally combining our limit with other independent PBH limits in the same mass range. We conclude the paper with section 4.4.

4.2 Flux ratio constraint

Dike et al. (2023) uses an Approximate Bayesian Computing Rubin (1984) approach to forward-modeling flux ratios from the four images of quads to constrain the mass fraction of PBH. This analysis is an extension of the flux ratio analysis framework constructed in Gilman et al. (2020b), Gilman et al. (2020a), and Gilman et al. (2019). The mass profile of the lensing galaxy is modeled as a power-law ellipsoid with external shear. Line-of-sight halos are modeled with a modified Sheth-Tormen halo mass function (Sheth et al., 2001b), while the halo substructure within the lensing galaxy itself is described by the subhalo mass function (SHMF),

$$\frac{d^2 N_{\rm sub}}{dm dA} = \frac{\Sigma_{\rm sub}}{m_0}\left(\frac{m}{m_0}\right)^{\alpha} \mathcal{F}(M_{\rm halo}, z), \tag{4.1}$$

where $\sum_{\rm sub}$ is the projected mass density, m_0 is the pivot mass, and $\mathcal{F}(M_{\rm halo}, z)$ is a function

to scale the number density of subhalos with main lensing halo mass and redshift as described in Gilman et al. (2020a). Values chosen for all of the parameters describing the lensing mass can be referred to in section 2.2 of Dike et al. (2023). PBH are rendered throughout the volume as point masses, and light from the source is raytraced through the modeled mass distribution to generate model flux ratios. These mass distributions are generated stochastically with the restriction that they fit the observed image positions, and the modeled flux ratios are compared to the observed via a summary statistic, therefore sampling the posterior.

4.3 Methods for improving constraints

Here we describe the three approaches we take to expand the work of Dike et al. (2023). First, we describe the increased sample we achieve by using quad lens systems observed by JWST. Second, we describe how we use this data as well as previous measurements to improve the constraint for those lenses with multiple measurements of the flux ratio. Third, we describe how we can combine our flux ratio constraint with those from alternative, independent PBH probes to achieve a better constraining power.

4.3.1 Increasing sample size

We aim to expand on the original dataset of eleven quads used in the analysis of Dike et al. (2023) using JWST MIRI imaging observations of thirty lenses consisting of both the quads in the original dataset and new candidate lenses (Nierenberg et al., 2021). The initial study uses a set of lenses observed in narrow-line, mid-infrared, or CO (10-11) emission selected for flux ratio analysis by Gilman et al. (2022b) with the requirement that the size of the source emission be large enough to avoid the effect of microlensing and time delay effects. Another requirement is that the lensing galaxy show no evidence for a disk structure (Hsueh et al. 2016, Hsueh et al. 2017, Gilman et al. 2017). The JWST observations probe a smaller scale around the emitting quasar, the extended dust emission region at 1-10pc (in comparison

to the typically 30-100pc narrow-line region), but this area is still large enough to avoid the effects of microlensing. The smaller scale of the source also allows for an increase in sensitivity because substructure of a lower mass is able to affect the deflection of the source.

The lenses and corresponding photometry references of the original dataset are flux ratios from the narrow-line emission of the [OIII] 4959 and 5007 Å doublet for B1422+231 (Nierenberg et al., 2014), HE0435-1223 (Nierenberg et al., 2017), PS J1606-2333, RX J0911+0551, WFI 2026-4536, WFI 2033-4723, WGD J0405-3308, WGD 2038-4008 (Nierenberg et al., 2020), and RX J1131-1231 (Sugai et al., 2007); mid-infrared flux ratios from PG1115+080; and CO (10-11) radio flux ratios from MG0414+0534 (Stacey & McKean 2018, Stacey et al. 2020).

4.3.2 Combining multiple flux ratio measurements

For the lenses that were already part of the sample of Dike et al. (2023), we plan to combine multiple measurements to get an increase in constraining power for each lens. To reduce computation time, we use the original flux ratio simulations and update the summary statistic:

$$S(r_{\rm model}, r_{\rm obs}) = \sqrt{\sum_{\rm i,j} (r_{\rm model(i)} - r_{\rm obs(i,j)})^2}. \tag{4.2}$$

Here the subscript i runs through each of the three flux ratios for each system, comparing $r_{\rm model}$, the flux ratio determined by the modeling process, and $r_{\rm obs}$, the flux ratio of each observation, and the subscript j runs through each observation.

4.3.3 Procedure for combining limits

Here we describe the procedure we follow to combine the strong lensing limit with statistically independent limits based on different diagnostics. Studies do not typically publish the full posterior distribution function of $f_{\rm PBH}$, so for simplicity we will assume that the pdfs are well

described by a semi-Gaussian centered on zero. The published limit L then correspond to the standard deviation of the Gaussian in the standard way

$$\int_0^{\mathrm{L}} \frac{2}{\sqrt{2\pi}\sigma_{\mathrm{L}}} e^{-\frac{x^2}{2\sigma_{\mathrm{L}}^2}} = 0.95, \tag{4.3}$$

for example, for a 95% limit. In this case, σ_{L} =L/2, and for a 68% limit, σ_{L}=L.

We take the measurements to be independent, assuming they all adopt a uniform prior on f_{PBH}, so the joint probability is a straightforward product of the probabilities. Therefore, the joint probability is a semi-gaussian with standard deviation σ_{T} given by

$$\frac{1}{\sigma_{\mathrm{T}}^2} = \sum_i \frac{1}{\sigma_i^2}, \tag{4.4}$$

where σ_i are the standard deviations of the individual measurements. It follows that for the joint limit $\mathrm{L_T}$,

$$\frac{1}{\mathrm{L_T^2}} = \sum_i \frac{1}{\mathrm{L}_i^2} \tag{4.5}$$

if the limits are at the same confidence level.

4.3.4 Limits

The analysis in Dike et al. (2023) gave a constraint of $f_{\mathrm{PBH}} < 17\%$ with a 95% confidence interval, so we can express as the strong lensing limit:

$$\mathrm{L_{SL}} = f_{\mathrm{PBH}}(M_{\mathrm{PBH}}) = 0.17 \qquad (10^4 M_\odot < M_{\mathrm{PBH}} < 10^6 M_\odot). \tag{4.6}$$

With the above procedure, we combine three additional PBH limits to the strong-lensing limit described in Section 4.2 within the mass range of 10^4-10^6 $\mathrm{M}_\odot$, the range of sensitivity of the Dike et al. (2023) study. These limits are summarized here briefly, and we encourage the reader to consult the original papers for more detail.

4.3.4.1 Wide Binary

A constraint on PBH can be placed by the observation of wide binaries that have not been disrupted by compact objects. A limit of this type was placed by Quinn et al. (2009) using a

sample of three wide binaries in the Galactic halo. We use the version of this limit published by Carr et al. (2010):

$$f_{\rm PBH}(M_{\rm PBH}) = 0.4 \qquad (10^3 M_\odot < M_{\rm PBH} < 10^8 M_\odot). \tag{4.7}$$

A key assumption noted in Quinn et al. (2009) is that the binary spends most of its orbit within the halo because a longer orbit away from this dense area will weaken the constraint.

4.3.4.2 Millilensing

Wilkinson et al. (2001) use a technique originally outlined in Press & Gunn (1973), putting a constraint on PBH from Very Long Baseline Array observations, looking for multiple images of 300 flat-spectrum radio sources from millilensing by compact objects. Here we reproduce the simplified form given by Carr et al. (2021) for this constraint:

$$f_{\rm PBH}(M_{\rm PBH}) = \begin{cases} \left(\frac{M_{\rm PBH}}{2x10^4 M_\odot}\right)^{-2} & (M_{\rm PBH} < 10^5 M_\odot) \\ 0.06 & (10^5 M_\odot < M_{\rm PBH} < 10^8 M_\odot). \end{cases} \tag{4.8}$$

The limit follows from the arguments in Kassiola et al. (1991) that a given number of compact sources in a volume will result in multiple images from gravitational lensing.

4.3.4.3 Large-Scale Structure

The formation of PBH could add a boost to the primordial matter power spectrum, and this boost was constrained by Lyman-α forest measurements in Afshordi et al. (2003). We use the form generalized by Mack et al. (2007) to include the possibility of PBH in a mixed dark matter model:

$$f_{\rm PBH}(M_{\rm PBH}) = \frac{10^4 M_\odot}{M_{\rm PBH}}. \tag{4.9}$$

The analysis, dependent on parameters describing the IGM flux transmission and temperature-density relation, predicts that the Poisson noise introduced to the matter power spectrum by PBH will result in a plateau towards higher wavenumbers k. Afshordi et al. (2003)

showed that the measurement of IGM flux transmission by McDonald et al. (2000) places a constraint on the abundance of PBH.

4.3.5 Result of combining limits

We have combined the limits described above into a new limit that has a stronger constraining power, especially in the region from $M_{\rm PBH} = 10^{4.4} - 10^{5.1} {\rm M}_{\odot}$ as shown in Figure 4.1. This limit is the most robust in this mass range given its dependence on multiple independent probes.

4.4 Discussion and conclusions

We show in this paper three methods for improving the mass fraction limit for PBH of intermediate mass. Two of these methods are focused expanding and refining the work in Dike et al. (2023) through increasing the quad sample size and combining multiple measurements of the same source. The third is to combine the limit of Dike et al. (2023) with other published limits in the same mass range. We find that this third method results in more stringent limits in this mass range than any method can accomplish on its own.

These are not the most constraining limits that exist within the mass range; however, our aim is to present the combination of independent limits as valuable strategy when one limit on its own may be dismissed as model-dependent.

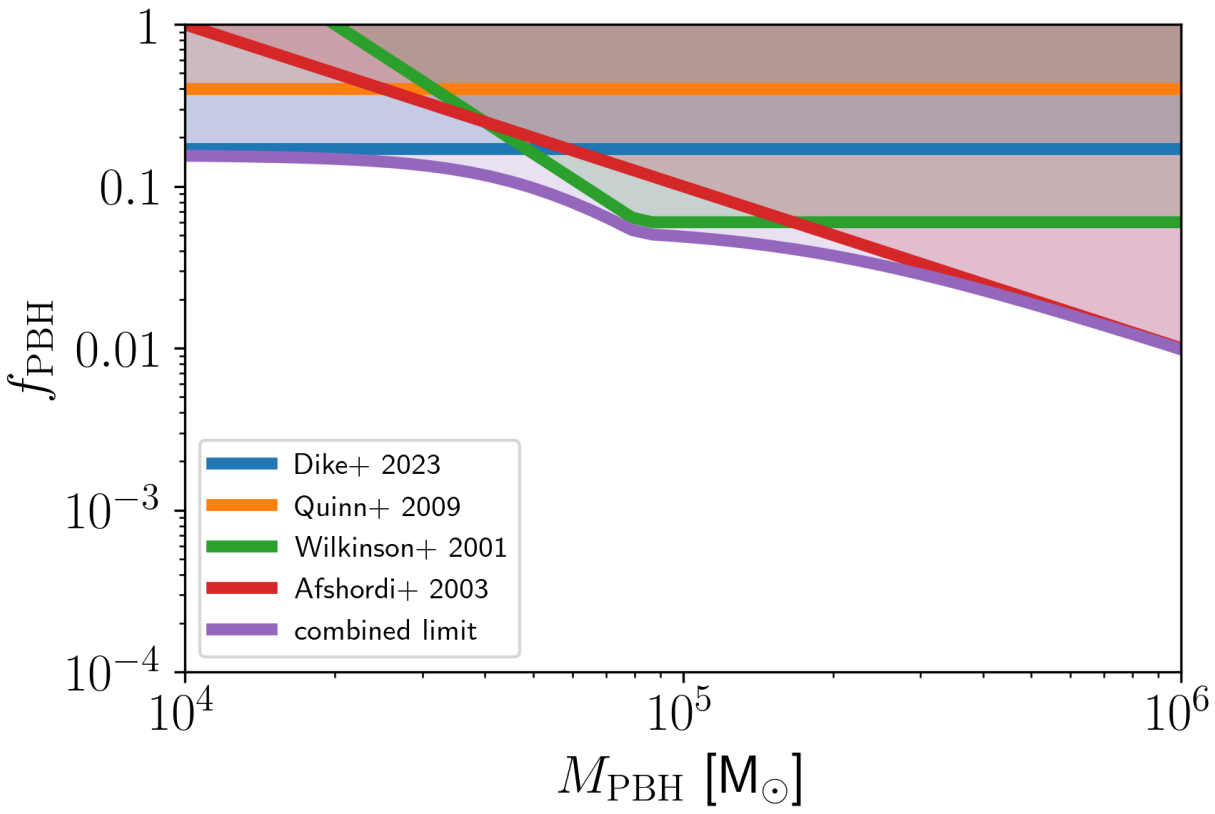

Figure 4.1: Exclusion plot of the intermediate-mass PBH constraints discussed in this paper along with the combined limit described in Section 4.3.3. Dike et al. (2023) is a limit from quad flux ratio analysis, Quinn et al. (2009) is a limit from the observed non-disruption of halo wide binaries, Wilkinson et al. (2001) is a limit from millilensing of compact radio objects, and Afshordi et al. (2003) is a limit placed by analysis of Ly-α forest observations.

CHAPTER 5

Conclusions

In this thesis, I presented results from two lines of inquiry. The first, detailed in Chapter 2, is an analysis of emission from the ground-vibrational state of SiO $J = 1 - 0, v = 0$ transition in the BAaDE survey, with a larger and more varied sample than any previous survey of this transition. The emission is faint and therefore found in nearby sources, which may explain the higher incidence of similarly faint isotopologue transition lines observed alongside the ground-vibrational state line, but there is a possibility that some quality of the maser pumping mechanism explains the co-occurrence. The expansion velocities are more varied than previous studies, likely because of the different source selection methods. The expansion velocities were found to be similar to CO in the cases where both types of emission were observed.

In the future, this work can be expanded upon with VLBI observations to confirm the location of the emission and provide further insight into the pumping mechanisms occurring around AGB stars. The previous study of de Vicente et al. (2016) found variability of this line to be chaotic and uncorrelated with any observed stellar pulsation cycle in their sample, and the BAaDE sample could similarly be monitored for time variability.

The second subject of this thesis was the effort to put constraints on PBH using flux-ratio anomalies from strongly lensed quads. The constraint that I present in Chapter 3, $f_{\rm PBH} < 0.17$ for $M_{\rm PBH} = 10^4$-$10^6 {\rm M}_\odot$ (95% C.L.), is independent of others in the same mass range. This constraint was obtained by forward modeling quad flux ratios for eleven lenses. In

Chapter 4, I set the groundwork for including new observations to this original sample to update the constraint. I presented a joint analysis using the flux-ratio anomaly limit along with three others in the same mass range, resulting in a more stringent limit.

The path forward for the work detailed in Chapters 3 and 4 includes incorporating the JWST observations of Nierenberg et al. (2021), which will also improve the mass sensitivity of the technique because the emitting region being observed is smaller. A surplus of new lens systems, expected to increase the sample of available lenses for this technique by an order of magnitude, are projected to be discovered in the near future by the survey telescope Euclid and Rubin Observatory's Legacy Survey of Space and Time (Oguri & Marshall 2010, Collett 2015). These observations will require follow-up observations using high-resolution instruments like Keck OSIRIS to be suitable for the flux-ratio analysis method. The same method presented here can also be used to constrain similar physics, such as ultradense minihalos that form alongside a population of PBH from the same primordial collapse mechanism (Delos & Silk, 2023). The applicability and sensitivity of the method will only improve as new lens data is collected.

Bibliography

Afshordi N., McDonald P., Spergel D. N., 2003, ApJ, 594, L71

Akeret J., Refregier A., Amara A., Seehars S., Hasner C., 2015, Journal of Cosmology and Astroparticle Physics, 2015, 043

Astropy Collaboration et al., 2013, A&A, 558, A33

Astropy Collaboration et al., 2018, AJ, 156, 123

Auger M. W., Treu T., Bolton A. S., Gavazzi R., Koopmans L. V. E., Marshall P. J., Moustakas L. A., Burles S., 2010, ApJ, 724, 511

Bailer-Jones C. A. L., 2015, PASP, 127, 994

Banik N., Bovy J., 2021, MNRAS, 504, 648

Banik U., van den Bosch F. C., Tremmel M., More A., Despali G., More S., Vegetti S., McKean J. P., 2019, MNRAS, 483, 1558

Belotsky K. M., et al., 2019, European Physical Journal C, 79, 246

Birrer S., Amara A., 2018, Physics of the Dark Universe, 22, 189

Birrer S., Amara A., Refregier A., 2017, J. Cosmology Astropart. Phys., 2017, 037

Birrer S., et al., 2021, Journal of Open Source Software, 6, 3283

Boboltz D. A., Claussen M. J., 2004, ApJ, 608, 480

Brandt T. D., 2016, ApJ, 824, L31

Cai R.-G., Chen T., Wang S.-J., Yang X.-Y., 2023, J. Cosmology Astropart. Phys., 2023, 043

Carr B. J., Hawking S. W., 1974, MNRAS, 168, 399

Carr B., Kühnel F., 2020, Annual Review of Nuclear and Particle Science, 70, 355

Carr B. J., Sakellariadou M., 1999, ApJ, 516, 195

Carr B., Silk J., 2018, MNRAS, 478, 3756

Carr B. J., Kohri K., Sendouda Y., Yokoyama J., 2010, Phys. Rev. D, 81, 104019

Carr B., Raidal M., Tenkanen T., Vaskonen V., Veermäe H., 2017, Phys. Rev. D, 96, 023514

Carr B., Clesse S., Garcia-Bellido J., Kuhnel F., 2019, arXiv e-prints, p. arXiv:1906.08217

Carr B., Kohri K., Sendouda Y., Yokoyama J., 2020, arXiv e-prints, p. arXiv:2002.12778

Carr B., Kohri K., Sendouda Y., Yokoyama J., 2021, Reports on Progress in Physics, 84, 116902

Carr B., Clesse S., Garcia-Bellido J., Hawkins M., Kuhnel F., 2023, arXiv e-prints, p. arXiv:2306.03903

Chandler C. J., de Pree C. G., 1995, ApJ, 455, L67

Chapline G. F., 1975, Nature, 253, 251

Chiba M., Minezaki T., Kashikawa N., Kataza H., Inoue K. T., 2005, ApJ, 627, 53

Cho S. H., Kaifu N., Ukita N., 1996, A&AS, 115, 117

Collett T. E., 2015, ApJ, 811, 20

Dalal N., Kochanek C. S., 2002, ApJ, 572, 25

Deguchi S., et al., 2004, PASJ, 56, 765

Deguchi S., et al., 2007, PASJ, 59, 559

Deguchi S., Nakashima J.-I., Zhang Y., Chong S. S. N., Koike K., Kwok S., 2010, PASJ, 62, 391

Delos M. S., Silk J., 2023, MNRAS, 520, 4370

Desmurs J. F., Bujarrabal V., Colomer F., Alcolea J., 2000, A&A, 360, 189

Despali G., Giocoli C., Angulo R. E., Tormen G., Sheth R. K., Baso G., Moscardini L., 2016, MNRAS, 456, 2486

Diamond P. J., Kemball A. J., 2003, ApJ, 599, 1372

Dickinson D. F., Reid M. J., Morris M., Redman R., 1978, ApJ, 220, L113

Diemer B., 2018, ApJS, 239, 35

Dike V., Morris M. R., Rich R. M., Lewis M. O., Quiroga-Nuñez L. H., Stroh M. C., Trapp A. C., Claussen M. J., 2021, AJ, 161, 111

Dike V., Gilman D., Treu T., 2023, MNRAS, 522, 5434

Dobler G., Keeton C. R., 2006, MNRAS, 365, 1243

Fiacconi D., Madau P., Potter D., Stadel J., 2016, ApJ, 824, 144

Fujii T., Deguchi S., Ita Y., Izumiura H., Kameya O., Miyazaki A., Nakada Y., 2006, PASJ, 58, 529

Gaia Collaboration et al., 2016, A&A, 595, A1

Gaia Collaboration et al., 2018, A&A, 616, A1

Gilman D., Agnello A., Treu T., Keeton C. R., Nierenberg A. M., 2017, MNRAS, 467, 3970

Gilman D., Birrer S., Treu T., Nierenberg A., Benson A., 2019, MNRAS, 487, 5721

Gilman D., Birrer S., Nierenberg A., Treu T., Du X., Benson A., 2020a, MNRAS, 491, 6077

Gilman D., Du X., Benson A., Birrer S., Nierenberg A., Treu T., 2020b, MNRAS, 492, L12

Gilman D., Bovy J., Treu T., Nierenberg A., Birrer S., Benson A., Sameie O., 2021, MNRAS, 507, 2432

Gilman D., Zhong Y.-M., Bovy J., 2022a, arXiv e-prints, p. arXiv:2207.13111

Gilman D., Benson A., Bovy J., Birrer S., Treu T., Nierenberg A., 2022b, MNRAS, 512, 3163

Gong J.-O., Kitajima N., 2017, J. Cosmology Astropart. Phys., 2017, 017

Green A. M., Kavanagh B. J., 2021, Journal of Physics G Nuclear Physics, 48, 043001

Greenhill L. J., Colomer F., Moran J. M., Backer D. C., Danchi W. C., Bester M., 1995, ApJ, 449, 365

Hawking S., 1971, MNRAS, 152, 75

Hawkins M. R. S., 2020, A&A, 633, A107

He Q., et al., 2022, MNRAS, 511, 3046

Herpin F., Baudry A., 2000, A&A, 359, 1117

Hsueh J. W., Fassnacht C. D., Vegetti S., McKean J. P., Spingola C., Auger M. W., Koopmans L. V. E., Lagattuta D. J., 2016, MNRAS, 463, L51

Hsueh J. W., et al., 2017, MNRAS, 469, 3713

Hsueh J. W., Enzi W., Vegetti S., Auger M. W., Fassnacht C. D., Despali G., Koopmans L. V. E., McKean J. P., 2020, MNRAS, 492, 3047

Hunter J. D., 2007, Computing in Science & Engineering, 9, 90

Inoue Y., Kusenko A., 2017, J. Cosmology Astropart. Phys., 2017, 034

Jewell P. R., Snyder L. E., Walmsley C. M., Wilson T. L., Gensheimer P. D., 1991, A&A, 242, 211

Josselin E., Loup C., Omont A., Barnbaum C., Nyman L. A., Sevre F., 1998, A&AS, 129, 45

Kainulainen K., Nurmi S., Schiappacasse E. D., Yanagida T. T., 2021, arXiv e-prints, p. arXiv:2108.08717

Kassiola A., Kovner I., Blandford R. D., 1991, ApJ, 381, 6

Khlopov M. Y., 2010, Research in Astronomy and Astrophysics, 10, 495

Kim J., Cho S.-H., Oh C. S., Byun D.-Y., 2010, ApJS, 188, 209

Kim J., Cho S.-H., Kim S. J., 2014, AJ, 147, 22

Koopmans L. V. E., 2005, MNRAS, 363, 1136

Kwan J., Scoville N., 1974, ApJ, 194, L97

Ladeyschikov D. A., Bayandina O. S., Sobolev A. M., 2019, AJ, 158, 233

Laroche A., Gilman D., Li X., Bovy J., Du X., 2022, MNRAS,

Lewis M. O., Pihlström Y. M., Sjouwerman L. O., Stroh M. C., Morris M. R., BAaDE Collaboration 2020, ApJ, 892, 52

Mack K. J., Ostriker J. P., Ricotti M., 2007, ApJ, 665, 1277

Mao S., Schneider P., 1998, MNRAS, 295, 587

McDonald P., Miralda-Escudé J., Rauch M., Sargent W. L. W., Barlow T. A., Cen R., Ostriker J. P., 2000, ApJ, 543, 1

McKinney W., 2010, in van der Walt S., Millman J., eds, Proceedings of the 9th Python in Science Conference. pp 51 – 56

Metcalf R. B., Madau P., 2001, ApJ, 563, 9

Miyoshi M., Matsumoto K., Kameno S., Takaba H., Lwata T., 1994, Nature, 371, 395

Morris M., 1975, ApJ, 197, 603

Morris M., 1985, in Morris M., Zuckerman B., eds, Astrophysics and Space Science Library Vol. 117, Mass Loss from Red Giants. pp 129–148, doi:10.1007/978-94-009-5428-1_13

Morris M., Alcock C., 1977, ApJ, 218, 687

Morris M., Redman R., Reid M. J., Dickinson D. F., 1979, ApJ, 229, 257

Moustakas L. A., Metcalf R. B., 2003, MNRAS, 339, 607

Müller-Sánchez F., Prieto M. A., Hicks E. K. S., Vives-Arias H., Davies R. I., Malkan M., Tacconi L. J., Genzel R., 2011, ApJ, 739, 69

Murgia R., Scelfo G., Viel M., Raccanelli A., 2019, Phys. Rev. Lett., 123, 071102

Navarro J. F., Frenk C. S., White S. D. M., 1997, ApJ, 490, 493

Nierenberg A. M., Treu T., Wright S. A., Fassnacht C. D., Auger M. W., 2014, MNRAS, 442, 2434

Nierenberg A. M., et al., 2017, MNRAS, 471, 2224

Nierenberg A. M., et al., 2020, MNRAS, 492, 5314

Nierenberg A., et al., 2021, A definitive test of the dark matter paradigm on small scales, JWST Proposal. Cycle 1, ID. #2046

Oguri M., Marshall P. J., 2010, MNRAS, 405, 2579

Passaglia S., Sasaki M., 2021, arXiv e-prints, p. arXiv:2109.12824

Planck Collaboration et al., 2020, A&A, 641, A6

Press W. H., Gunn J. E., 1973, ApJ, 185, 397

Quinn D. P., Wilkinson M. I., Irwin M. J., Marshall J., Koch A., Belokurov V., 2009, MNRAS, 396, L11

Quiroga-Nuñez L. H., et al., 2020, arXiv e-prints, p. arXiv:2009.01909

Rubin D. B., 1984, The Annals of Statistics, 12, 1151

Sasaki M., Suyama T., Tanaka T., Yokoyama S., 2018, Classical and Quantum Gravity, 35, 063001

Schmidt T., et al., 2022, arXiv e-prints, p. arXiv:2206.04696

Sevenster M. N., Chapman J. M., Habing H. J., Killeen N. E. B., Lindqvist M., 1997, A&AS, 122, 79

Sevenster M. N., van Langevelde H. J., Moody R. A., Chapman J. M., Habing H. J., Killeen N. E. B., 2001, A&A, 366, 481

Shajib A. J., et al., 2022, arXiv e-prints, p. arXiv:2202.11101

Sheth R. K., Mo H. J., Tormen G., 2001a, MNRAS, 323, 1

Sheth R. K., Mo H. J., Tormen G., 2001b, MNRAS, 323, 1

Sisson S. A., Fan Y., Beaumont M., 2018, Handbook of approximate Bayesian computation. CRC Press

Sjouwerman L. O., Capen S. M., Claussen M. J., 2009, ApJ, 705, 1554

Sjouwerman L. O., Pihlström Y. M., Rich R. M., Morris M. R., Claussen M. J., 2017, in Crocker R. M., Longmore S. N., Bicknell G. V., eds, IAU Symposium Vol. 322, The Multi-Messenger Astrophysics of the Galactic Centre. pp 103–106, doi:10.1017/S1743921316012394

Sjouwerman L. O., Pihlström Y. M., Rich R. M., Claussen M. J., Morris M. R., BAaDE Collaboration 2018, in Tarchi A., Reid M. J., Castangia P., eds, Vol. 336, Astrophysical Masers: Unlocking the Mysteries of the Universe. pp 180–183, doi:10.1017/S1743921317009292

Snyder L. E., Buhl D., 1974, ApJ, 189, L31

Sobolev V. V., 1960, Moving envelopes of stars

Soria-Ruiz R., Alcolea J., Colomer F., Bujarrabal V., Desmurs J. F., Marvel K. B., Diamond P. J., 2004, A&A, 426, 131

Springel V., et al., 2008, MNRAS, 391, 1685

Stacey H. R., McKean J. P., 2018, MNRAS, 481, L40

Stacey H. R., Lafontaine A., McKean J. P., 2020, MNRAS, 493, 5290

Stroh M. C., Pihlström Y. M., Sjouwerman L. O., Claussen M. J., Morris M. R., Rich M. R., 2018, ApJ, 862, 153

Stroh M. C., Pihlström Y. M., Sjouwerman L. O., Lewis M. O., Claussen M. J., Morris M. R., Rich R. M., 2019, ApJS, 244, 25

Sugai H., Kawai A., Shimono A., Hattori T., Kosugi G., Kashikawa N., Inoue K. T., Chiba M., 2007, ApJ, 660, 1016

Trapp A. C., Rich R. M., Morris M. R., Sjouwerman L. O., Pihlström Y. M., Claussen M., Stroh M. C., 2018, ApJ, 861, 75

Treu T., 2010, ARA&A, 48, 87

Vegetti S., Koopmans L. V. E., Bolton A., Treu T., Gavazzi R., 2010, MNRAS, 408, 1969

Viel M., Becker G. D., Bolton J. S., Haehnelt M. G., 2013, Phys. Rev. D, 88, 043502

Villasenor B., Robertson B., Madau P., Schneider E., 2022, arXiv e-prints, p. arXiv:2209.14220

Virtanen P., et al., 2020, Nature Methods, 17, 261

Walt S. v. d., Colbert S. C., Varoquaux G., 2011, Computing in Science & Engineering, 13, 22

Weyant A., Schafer C., Wood-Vasey W. M., 2013, ApJ, 764, 116

Wilkinson P. N., et al., 2001, Phys. Rev. Lett., 86, 584

Wizinowich P., et al., 2022, in Schreiber L., Schmidt D., Vernet E., eds, Society of Photo-Optical Instrumentation Engineers (SPIE) Conference Series Vol. 12185, Adaptive Optics Systems VIII. p. 121850Q, doi:10.1117/12.2628275

Wright S., et al., 2019, in Bulletin of the American Astronomical Society. p. 201

Xu G., Ostriker J. P., 1994, ApJ, 437, 184

Zel'dovich Y. B., Novikov I. D., 1967, Soviet Ast., 10, 602

Zhou H., Li Z., Liao K., Niu C., Gao H., Huang Z., Huang L., Zhang B., 2021, arXiv e-prints, p. arXiv:2109.09251

Zhou H., Lian Y., Li Z., Cao S., Huang Z., 2022, MNRAS, 513, 3627

de Vicente P., et al., 2016, A&A, 589, A74